

Spatially-Resolved Temperature and Density Structures of Nearby HII regions

YIFEI JIN (金刈非)^{1,2} RALPH SUTHERLAND,¹ LISA J. KEWLEY,^{1,3,2} AND DAVID C. NICHOLLS^{1,2}

¹*Research School for Astronomy & Astrophysics, Australian National University, Canberra, Australia, 2611*

²*ARC Centre of Excellence for All Sky Astrophysics in 3 Dimensions (ASTRO 3D)*

³*Institute for Theory and Computation, Harvard-Smithsonian Center for Astrophysics, Cambridge, MA 02138, USA*

(Received January 1, 2018; Revised January 7, 2018; Accepted October 4, 2023)

Submitted to ApJ

ABSTRACT

Photoionization models frequently assume constant temperature or density within HII regions. We investigate this assumption by measuring the detailed temperature and density structures of four HII regions in the Large Magellanic Cloud and the Small Magellanic Cloud, using integral-field spectroscopic data from the Wide-Field Spectrograph on the ANU 2.3m telescope. We analyse the distribution of emission-lines of low-ionization species, intermediate-ionization species and high-ionization species. We present the complex electron temperature and density structures within HII regions. All four nebulae present a negative gradient in the electron density profile. Both positive and negative temperature gradients are observed in the nebulae. We create a series of nebula models with a constant ISM pressure and varying temperature and density distributions. Comparison of the line ratios between our HII regions and models suggests that none of the simple nebula models can reproduce the observed temperature and density structures. Comparison between the models and the data suggests that the ISM pressure of nebulae in LMC and SMC is between $\log(P/k)=6-7.5$. Complex internal structures of the nebulae highlight the importance of future Monte-Carlo photoionization codes for accurate nebula modeling, which include a comprehensive consideration of arbitrary geometries of HII regions.

Keywords: ISM: HII regions — ISM: structure — galaxies:starburst

1. INTRODUCTION

To fully understand galaxies, we need to accurately model the HII regions within galaxies. The electron temperature and density are two of the fundamental quantities that determine the nebular emission-line spectrum within HII regions. Accurate predictions of the interstellar medium (ISM) physical quantities rely on the assumed or modeled distributions of electron temperature, T_e , and density, n_e .

The ISM electron temperature and density distributions across HII regions are complex. The density distributions in most HII regions show filamentary or shell-like structures (Kennicutt 1984). The density measurements within these structures have diverse radial gradients (Binette et al. 2002; Herrera-Camus et al.

2016; Rubin et al. 2016), although relatively uniform density distributions are seen in some cases (Garnett & Dinerstein 2001; Krabbe & Copetti 2002; García-Benito et al. 2010). Surveys of both galactic and extragalactic HII regions indicate that approximately half the HII regions have internal variations in electron density (Copetti et al. 2000; Malmann et al. 2002).

The presence of temperature fluctuations in HII regions is under significant debate due to the notorious difficulty in measuring the electron temperature. Some studies show evident temperature fluctuations (Peimbert et al. 2004; Hägele et al. 2006; Kewley et al. 2019b), while others find no temperature fluctuations (Stasińska et al. 2013; Liu et al. 2006).

The underlying temperature and density structures in HII regions affect the robustness of metallicity calibrations. The most direct calibration method is to convert metallicities from electron temperatures in the O²⁺ zone after correcting for the unseen ionization stages (the so-

called ionization correction factor, ICF). The ICF is determined from the photoionization models under the assumption of constant electron temperature and density across the HII region. Hägele et al. (2008) find electron temperature variations raise the uncertainty of metallicities by up to 0.2 dex through the ICF method.

The temperature variation is one of the potential causes of the discrepancies among metallicities measured from different emission-lines (Kewley et al. 2019b). Commonly used metallicity-sensitive emission-line ratios are $([\text{O II}]\lambda 3727 + [\text{O III}]\lambda\lambda 4959, 5007)/\text{H}\beta$ (known as R_{23}), $[\text{O III}]\lambda 5007/\text{H}\beta/[\text{N II}]\lambda 6584/\text{H}\alpha$ (known as O3N2) and $[\text{N II}]\lambda 6584/\text{H}\alpha$. Recombination lines give larger metallicities than auroral lines. The offset between recombination line and auroral metallicities has been suggested as arising from temperature fluctuations in HII regions (Peimbert 1967), which is known as the abundance discrepancy factor (ADF).

The ISM pressure incorporates the complex structures of electron temperature and density. Constant pressure models are applicable to the majority of HII regions where the sound-crossing time is shorter than the heating and cooling timescale. Pressure photoionization models with complex temperature and density structures have been successfully applied to galaxies at $z \sim 2$, suggesting the existence of the high-pressure HII regions in high- z galaxies (Lehnert et al. 2009).

Current photoionization models significantly underestimate the complexity of the internal structures of HII regions. Isothermal or constant density ISM conditions are often assumed in photoionization models. Isothermal models with a single temperature across the nebula have been used in calibrating the standard density-sensitive line ratios (Osterbrock 1989; Rubin et al. 1994), and determining the excitation power source in galaxies (Filippenko 1985; Groves et al. 2004). The constant density distribution assumption is adopted in measuring the electron temperature and density in HII regions (Osterbrock 1989). The constant density assumption is also used in deriving the metallicities measured from auroral lines. In modern constant pressure models, the majority of modeled HII regions produce complex internal gradients in electron temperature and density, while only few specific cases with $\log(\text{O}/\text{H})+12 \sim 8.23$ can be approximated with the isothermal or constant density conditions (Kewley et al. 2019a).

Nearby HII regions are laboratories for understanding the internal structure of the ISM electron temperature and density. With the advantage of proximity, the Magellanic Clouds provide a rich reservoir of HII regions for better understanding the ISM temperature and density fluctuations (Kennicutt 1984; Kennicutt & Hodge

1986; Chu & Kennicutt 1986; Vermeij & van der Hulst 2002; Peña-Guerrero et al. 2012b). Integral-field unit (IFU) observations offers highly spatially-resolved data of HII regions in the Magellanic Clouds for the detailed study of electron temperature and density structures (Dopita & Seitzzahl 2019; Kumari et al. 2017). Future IFU data sets of nearby HII regions will be released in the on-going TYPHOON program (Seibert et al. in prep.) and the up-coming SDSS-V/Local Volume Mapper (LVM) (Kollmeier et al. 2017).

In this paper, we present deep IFU observations of four HII regions in the Large Magellanic Cloud (LMC) and the Small Magellanic Cloud (SMC). The data were obtained using the Wide-Field Spectrograph (WiFeS) with grating resolution of $R \sim 7000$. We derive the electron temperature and density with the deep IFU data, and further analyze the thermal and density structures within each HII region using the highly spatially-resolved datacube. This is the first study of nebular internal structures with a sample of LMC/SMC nebulae using the IFU data with a resolution of 0.2 – 0.3 pc. This paper is structured as below. We first describe the sample of HII regions in Section 2 and describe the data and the data reduction in Section 3. We describe the calibrations of electron temperature, density and pressure in Section 4. We present the electron temperature and density structures of HII regions in Section 5. In Section 6, we compare our HII regions with the pressure photoionization models. The discussion is given in Section 7.

2. THE SAMPLE

The four HII regions are selected from a series of spatially-resolved observations of the nebulae in the Magellanic Clouds (Dopita et al. 2016, 2018). The four HII regions are bright and young compact HII regions ionized by a single O-star or simple star clusters. Three HII regions, N456, N77A and N88A are from SMC, and one, N191A, is from LMC. The simple ionizing sources make these compact HII regions ideal targets for testing current photoionization models. The compact size ($\sim 10''$ in diameter) and proximity allows these compact HII regions to fit within the WiFeS field of the view (FoV). Some fundamental physical quantities derived from the global spectra of these HII regions are listed in Table 1.

LMC N191 is a complex HII region which presents two components in $\text{H}\alpha$, $[\text{O III}]$ and $\text{H}\beta$ narrow band images (Henize 1956). N191A is more compact and brighter between the two components, which has a diameter of $5''.2$ (1.2 pc at LMC distance) (Selier & Heydari-Malayeri 2012). The broad V -band image reveals that the ion-

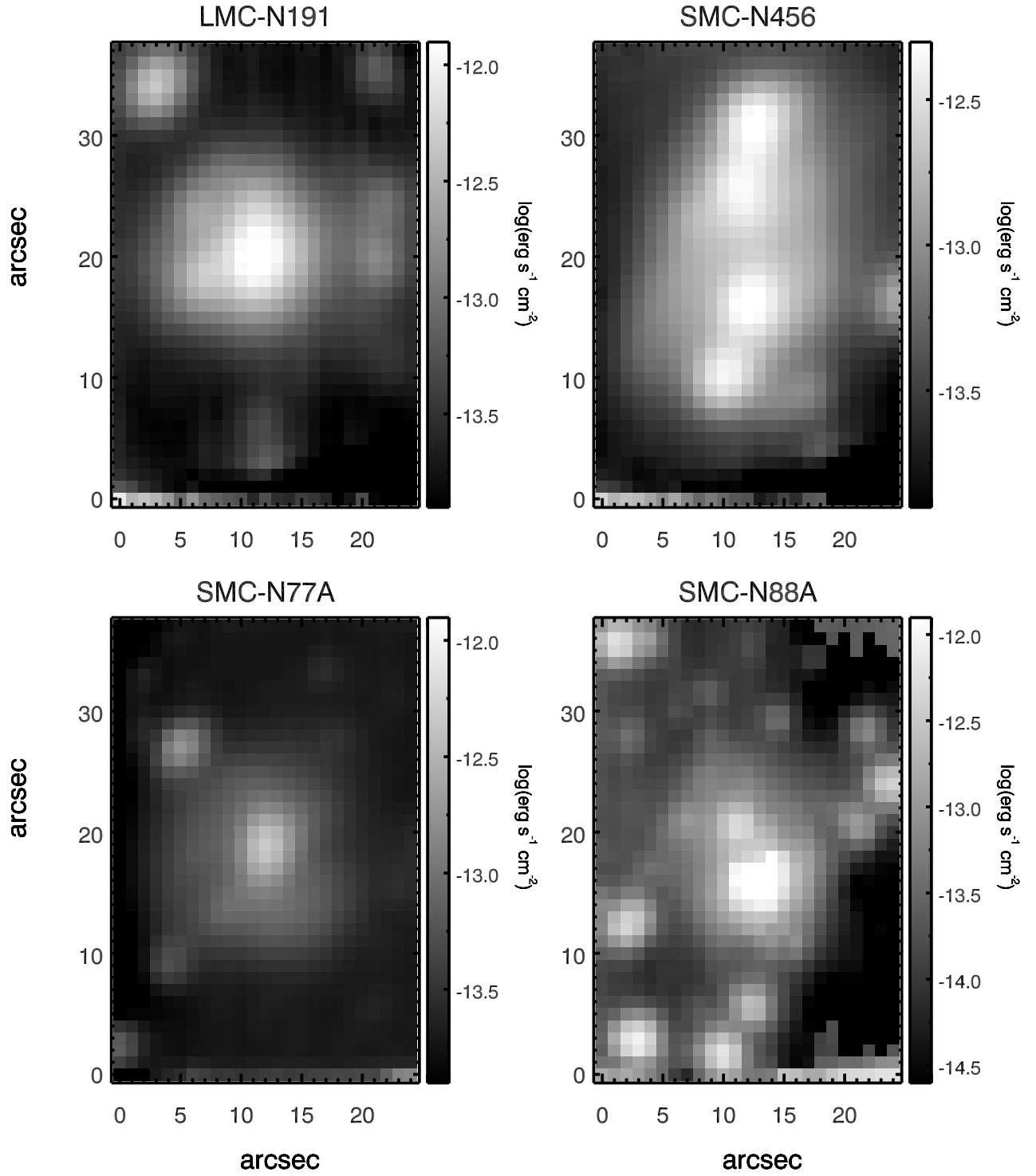


Figure 1. Collapsed IFU images of four HII regions in LMC and SMC. The field of view is $25'' \times 38''$. Grey scale color indicates the line-of-sight integrated flux.

Table 1. The fundamental physics quantities of the HII region sample ^a

HII Region	Size	A_V	T_e	n_e
	pc	mag	K	cm^{-3}
LMC N191A	1.2	~ 2.70	10,800	600
SMC N77A	2.9	~ 0.25	14,240	60
SMC N88A	1.2	~ 1.38	$\sim 14,100$	2870
SMC N456	–	–	$\sim 12,000$	~ 100

^aThe data are collected from the literature Selier & Heydari-Malayeri (2012) for LMC N191A and SMC N77A, Testor et al. (2003) for SMC N88A and Peña-Guerrero et al. (2012a) for SMC N456.

ized gas in N191A is excited by an O-star located at the center of the nebula (Selier & Heydari-Malayeri 2012).

SMC N77A is a spherical HII region having a radius of $10''$ (Selier & Heydari-Malayeri 2012). A dust lane crosses SMC N77A along the east-west direction (Selier & Heydari-Malayeri 2012; Toribio San Cipriano et al. 2017). The major ionizing source of N77A is a B-star residing north of the dust lane. The average extinction of N77A is $A_V \sim 0.25$ mag (Selier & Heydari-Malayeri 2012).

SMC N88A is the brightest HII region in the SMC (Testor et al. 2003). N88A is a ~ 1 -pc sized ionized gas “blob” excited by an O3-4 star (Testor et al. 2003). The heavy dust core in N88A produces its high integral extinction of $A_V = 1.38$ mag (Garnett et al. 1995; Testor et al. 2003).

SMC N456 is the second brightest HII region in the SMC (Peimbert & Torres-Peimbert 1976), with an inhomogeneous thermal structure. Long-slit spectrographic study indicates the mean-square temperature variation, t^2 (first introduced by Peimbert (1967)), in SMC N456 is 0.067 ± 0.013 (Peña-Guerrero et al. 2012a).

3. OBSERVATION AND DATA REDUCTION

The spectroscopic data were observed using WiFeS. WiFeS (Dopita et al. 2007, 2010) is an image-slicing integral-field spectrograph mounted at the Australian National University 2.3 m telescope at the Siding Spring Observatory. WiFeS has a $25'' \times 38''$ field of the view with spaxels each $1 \times 1''$ in angular size. The double-beam spectrograph feeds the light into the blue and red cameras simultaneously to cover the wavelength ranging from 3300 to 9000 Å. We used the high-resolution grat-

ings of $R = 7000$ by splitting the spectra into U , B , R and I bands.

The observations were taken between November and December 2015 with seeing FWHM 1.0-2.0 arcsec. Each HII region was observed using 10, 100 and 1000 (or 800) second exposures. The longer exposures were aimed at securing flux measurements of faint emission lines down to $\sim 10^{-5}$ of the $H\beta$ flux. The shorter exposures were necessary to minimize the saturation on the bright hydrogen and oxygen lines.

The data were reduced using the standard WiFeS pipeline, PyWiFeS (Childress et al. 2014). Telluric lines were removed by subtracting observed clear sky regions adjacent to the HII regions, from each observation. The separate camera spectra were then combined using the overlapping spectral regions between adjacent cameras. The final data has a spectral resolution of 43 kms^{-1} and a spatial resolution of 0.3 pc for SMC N77A, SMC N88A and SMC N456, and a spatial resolution of 0.24 pc for LMC N191A.

4. DERIVED QUANTITIES

4.1. Emission-line maps

The emission-line fluxes are obtained from each pixel by integrating the spectrum subtracted from the underlying stellar continuum and nebular continuum. Continuum components are estimated by using the average flux over a 10\AA wavelength interval on either the left side or the right side to each emission-line. In Figure 2 to Figure 5, we show maps of the emission-lines representing species in the high-ionization zone, the intermediate-ionization zone and the low-ionization zone of the nebula. We use the Balmer lines to trace the main body of HII regions. The $[\text{O III}]\lambda 5007$ and $[\text{Ne III}]\lambda 3869$ lines are used to trace the high-ionization zone. The $[\text{Ar III}]\lambda 7136$ and $[\text{S III}]\lambda 6312$ lines are the tracers of the intermediate-ionization zone. The $[\text{O II}]\lambda 3727$, $[\text{N II}]\lambda 6584$ and $[\text{S II}]\lambda 6716$ emission-lines are used to trace the low-ionization zone of the nebula. The boundary of the HII region is identified at the pixels with $\text{Flux}(H\alpha) = 10\% \text{Flux}(H\alpha)_{\text{peak}}$, where $\text{Flux}(H\alpha)_{\text{peak}}$ is the maximal $H\alpha$ flux.

In Figure 2 to Figure 5, a clear spatial segregation exists among different ionization zones. The high-ionization zone that is traced by $[\text{O III}]\lambda 5007$ and $[\text{Ne III}]\lambda 3869$ is compact around the nebular center because of the hard ionization field from the ionizing star in proximity to the star. In contrast, the low-ionization zone traced by $[\text{O II}]\lambda 3727$, $[\text{N II}]\lambda 6584$ and $[\text{S II}]\lambda 6716$ is located at the boundary of the HII regions. The $[\text{Ar III}]\lambda 7136$ and $[\text{S III}]\lambda 6312$ lines are located between the high-ionization and low-ionization zones.

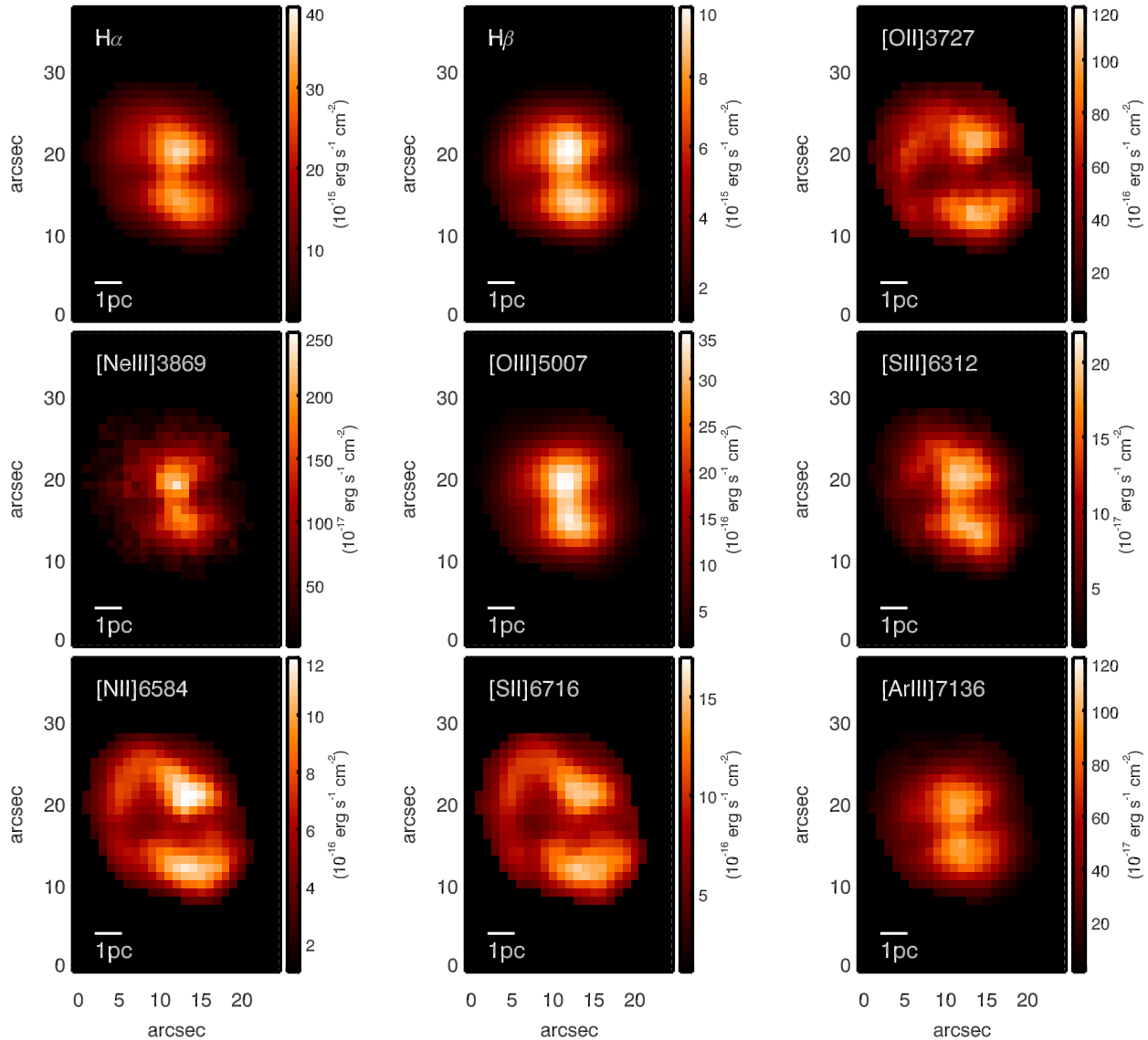


Figure 2. Emission-line maps of SMC N77A. We show the maps of Balmer lines $H\alpha$ and $H\beta$, the emission-lines of high-ionization species $[O\ III]\lambda 5007$ and $[Ne\ III]\lambda 3869$, the emission-lines of intermediate-ionization species $[Ar\ III]\lambda 7136$, $[S\ III]\lambda 6312$, and the emission-lines of low-ionization species $[O\ II]\lambda 3727$, $[N\ II]\lambda 6584$ and $[S\ II]\lambda 6716$.

Our HII region sample presents diverse nebular morphologies. The emission-lines in LMC N191 have an extended morphology, which is consistent with the early $H\alpha$ image observed by [Henize \(1956\)](#). SMC N88A appears as a bright compact point source for the emission-lines of high-ionization and intermediate-ionization species, which is consistent with the near-infrared imaging of SMC N88A ([Testor et al. 2010](#)). For the emission-lines of low-ionization species, an extended region exists north-east of the bright nebular center. SMC N456 presents a shell-like morphology for the emission-lines of low-ionization species. However, the emission-lines

of high-ionization species present a spherical morphology. The extended morphology of SMC N456 is also confirmed in [Arellano-Córdova & Rodríguez \(2020\)](#). SMC N77A appears to have a two-lobe morphology for emission-lines of high-ionization and intermediate-ionization species, which is split by a dust lane crossing from east to west ([Selier & Heydari-Malayeri 2012](#)). For the low-ionization species, the emission-lines are located on the nebular edge, leading to a shell-like morphology.

4.2. Extinction Correction

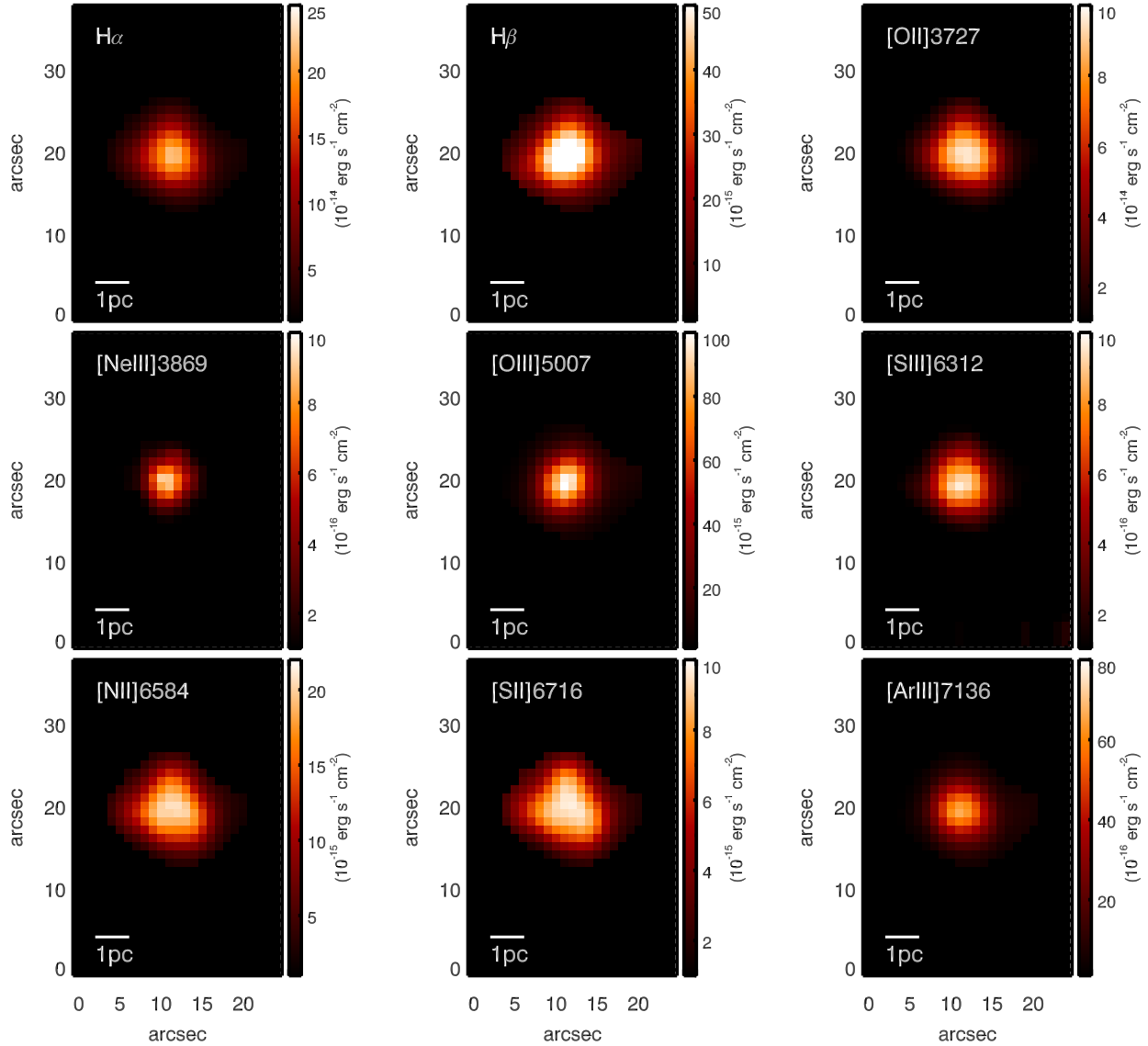


Figure 3. Same as Figure 2 but for LMC N191.

The extinction correction is carried out through the $H\alpha/H\beta$ Balmer decrement, using the [Fitzpatrick \(1999\)](#) extinction law. We select a $R_V = 3.16$ for nebula in LMC and $R_V = 2.93$ for nebula in SMC ([Pei 1992](#)). The Fitzpatrick extinction curve is a generally-used parameterized curve. Compared to the average extinction curves of the LMC and the SMC ([Gordon et al. 2003](#)), we find the difference of the extinction corrected fluxes is 0.7%-8% by applying different extinction curves on our sample.

Figure 6 presents maps of the derived A_V with the distribution of $H\beta$ fluxes. We notice that the enhancement of $A_V \sim 0.7$ mag in the SMC N77A is at the position of

the central dust lane. In SMC N88A, the maximum A_V is ~ 2.5 mag, located at the peak of $H\beta$ fluxes.

4.3. Determining electron density

We measure the electron density, n_e , for each resolution element by using the calibrations in [Osterbrock & Ferland \(2006\)](#) (hereafter OF06) based on single-atom fixed temperature, fixed density models, and the diagnostics given by [Kewley et al. \(2019a\)](#) (hereafter K19) based on their theoretical density models. Compared with single-atom models, the density models in [Kewley et al. \(2019a\)](#) are more representative to the physical conditions in nebulae in terms of the temperature structures changing with the ionization field and the metallicity. The elec-

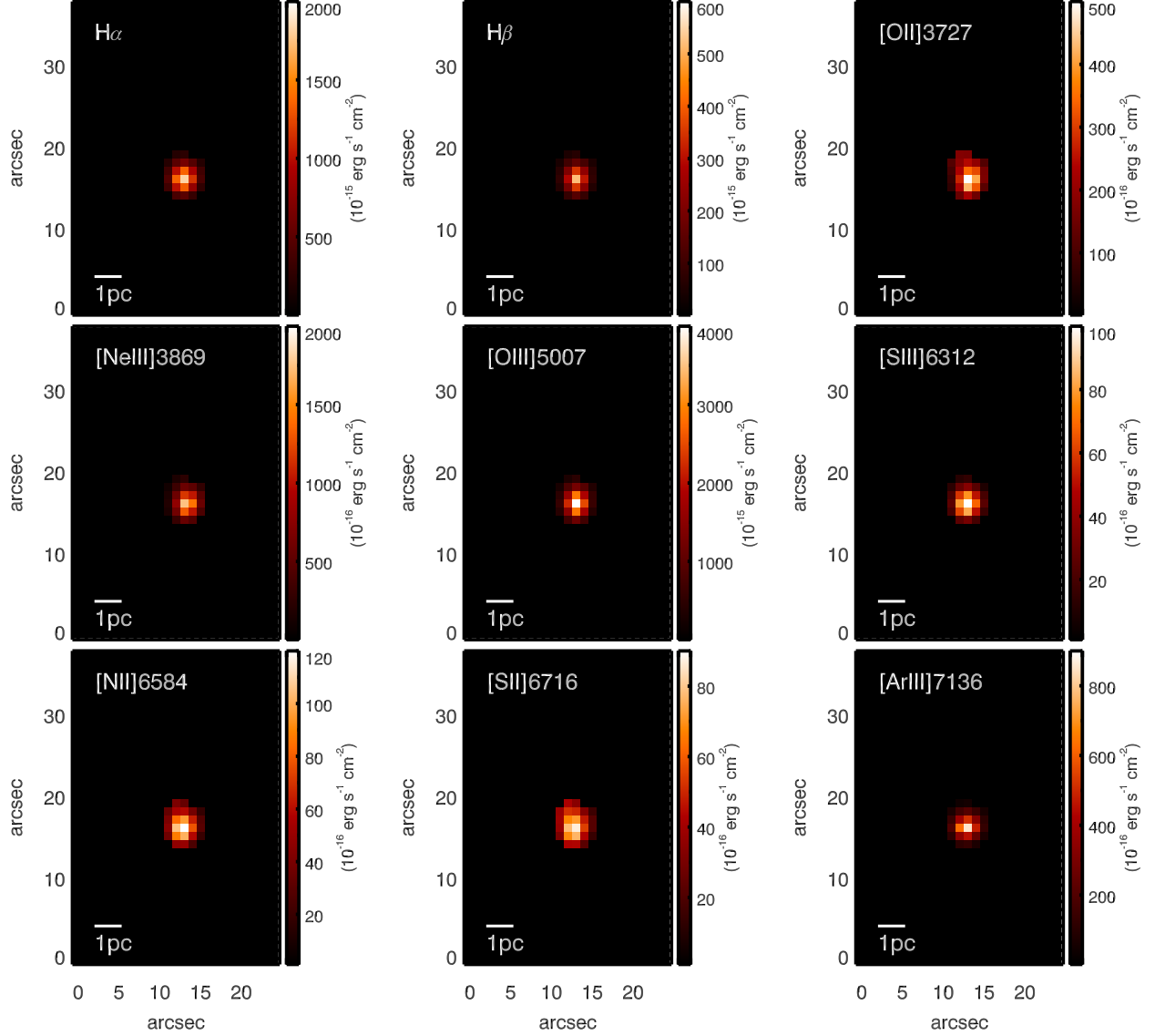


Figure 4. Same as Figure 2 but for SMC N88A.

tron densities derived from the [Osterbrock & Ferland \(2006\)](#) method and the [Kewley et al. \(2019a\)](#) density models are independent from the ISM pressure, which can be used to compare with the constant pressure models where the ISM pressure is a free parameter.

The electron densities are derived from the $[\text{S II}]\lambda 6716 / [\text{S II}]\lambda 6731$ ratio and the $[\text{O II}]\lambda 3726 / [\text{O II}]\lambda 3729$ ratio respectively. We use the amplitude-to-noise (A/N) ratio to describe the quality of each emission-line. The A/N ratio is the ratio of the peak of emission-line flux to the noise of emission-lines, tracing both the signal-to-noise ratio and the strength of emission-line fluxes. The A/N ratio is sensitive to the emission-lines with low signal-to-

noise ratios but evident excess of fluxes superimposed on the continuum. We require A/N of the $[\text{O II}]$ doublets and the $[\text{S II}]$ doublets larger than 5 in each spaxel.

The OF06 models use the atomic data from [Mendoza \(1983\)](#), which provides a compilation of transition probabilities, electron excitation coefficients and photoionization cross sections from sophisticated computation and measurements. The K19 models use the CHIANTI v.8.0 atomic data ([Del Zanna et al. 2015](#)) in conjunction with the energy level information of each ions from NIST database. The K19 models are suitable for calculating the electron density between 1 and 10^8 cm^{-3} .

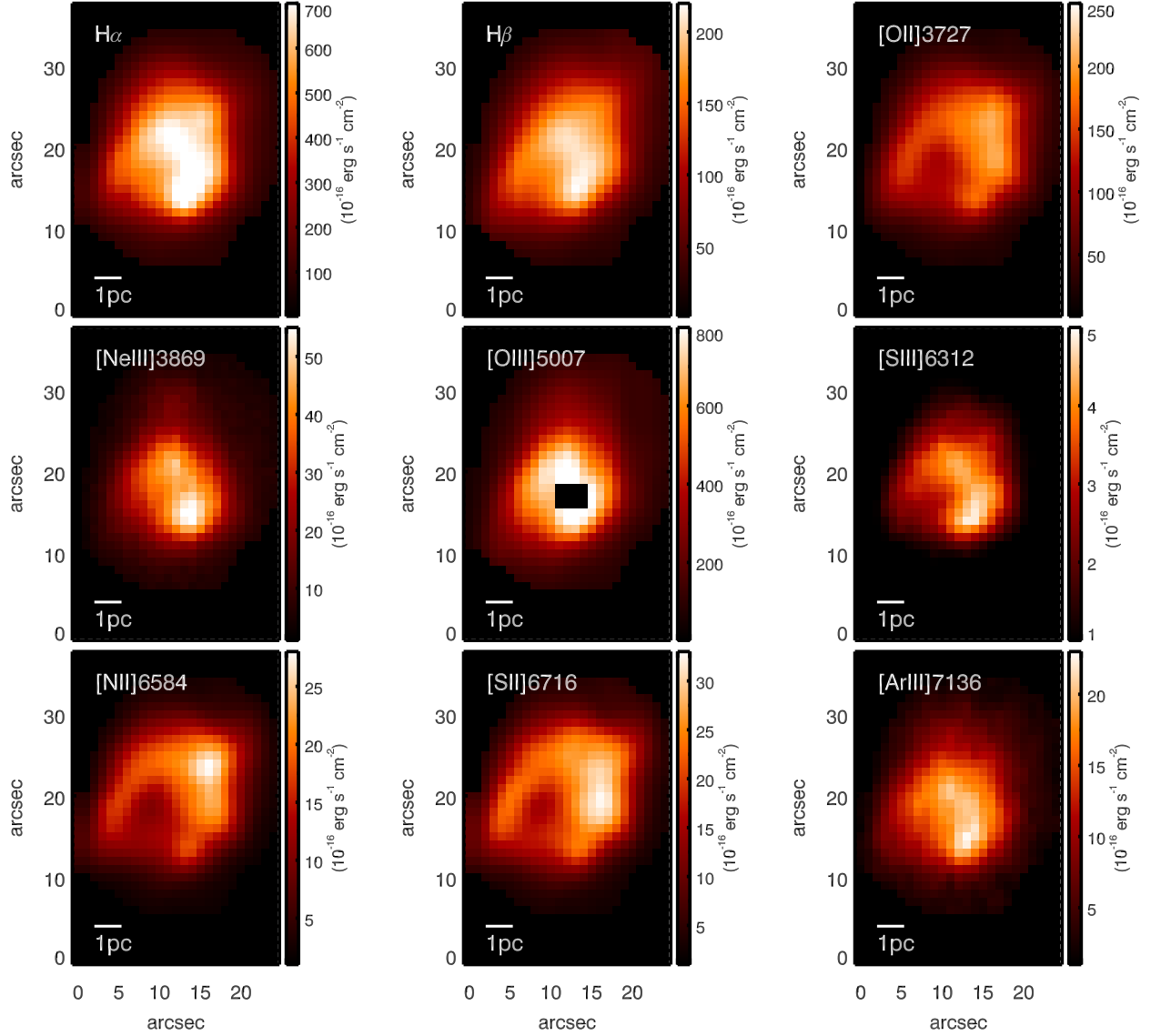


Figure 5. Same as Figure 2 but for SMC N456. The central pixel in the [O III] λ 5007 map is a bad pixel because the [O III] λ 5007 is saturated at the center of SMC N456.

4.4. Determining electron temperature

We measure the electron temperatures, T_e , from collisional lines using the method described in Osterbrock & Ferland (2006) and the calibration in Nicholls et al. (2020) (hereafter NKS20). The Osterbrock & Ferland (2006) method is a simple polynomial fit to the single-atom models within a temperature range from 5000 K to 25,000 K. Nicholls et al. (2020) re-calibrate the relationship between the [O III] emission-line ratios and T_e by using a rational polynomial as shown in equation 1

$$\log_{10}(T_e) = \frac{P_0 + P_1x + P_2x^2}{1 + Q_1x + Q_2x^2 + Q_3x^3}, \quad (1)$$

where x is $\log_{10}([\text{O III}]\lambda 4363/[\text{O III}]\lambda\lambda 4959, 5007)$, and $P_0, P_1, P_2, Q_1, Q_2, Q_3$ are the fit coefficients. We require $A/N > 5$ for [O III] $\lambda\lambda$ 4959,5007 and [O III] λ 4363

The OF06 models use the atomic data from Mendoza (1983). The NKS20 models use the CHIANTI v.8.0 atomic data (Del Zanna et al. 2015) in conjunction with the energy level information of each ions from NIST database.

4.5. Determining P/k

The pressure within HII regions is derived from the temperature, T , and the particle density, n , of nebula through the ideal gas assumption $P = nkT$. We assume

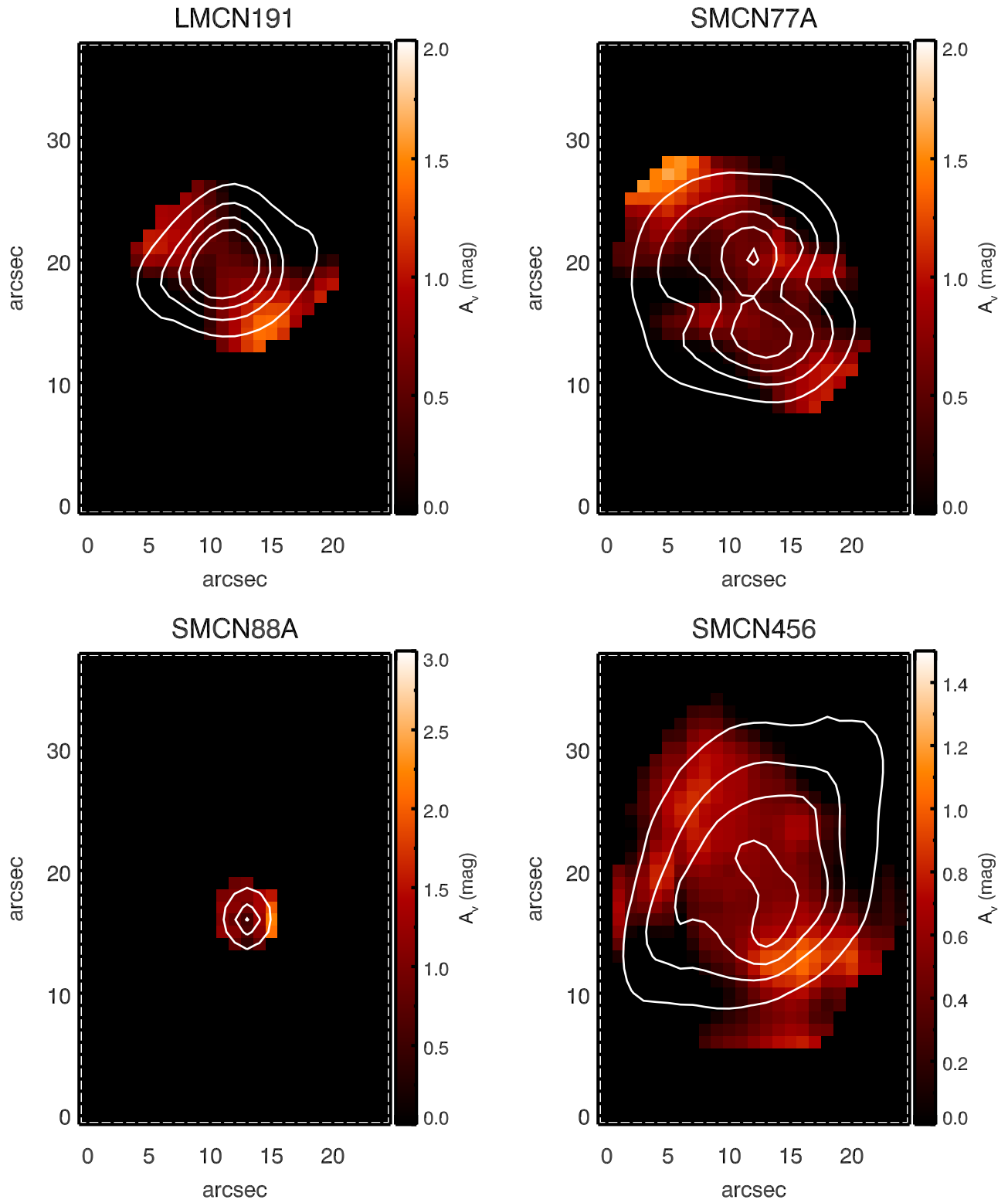


Figure 6. Maps of attenuation A_V . The color code indicates the value of A_V . The white contours present the distribution of $H\beta$ emission-line fluxes.

that $T \equiv T_e$ and approximate the total particle density n from the electron density n_e through $n \sim 2n_e(1+He/H)$ given hydrogen and helium are the majority species in HII regions. Finally, the nebular pressure is derived through $P/k = 2n_e(1 + He/H)T_e$.

5. ANALYSIS

5.1. Electron density structures

In Figure 7 and Figure 8, we present the maps of electron density derived from the [O II] ratio, $n_e(\text{OII})$, and the [S II] ratio, $n_e(\text{SII})$. In LMC N191, SMC N77A and SMC N88A, the 2D density distribution has a dense core at the center of the nebula and the density decreases along the radius of nebula. In SMC N456, there are three dense clumps located at three corners of the nebula.

We measure the gradients of the electron density profiles using the following function,

$$\frac{n_e}{\text{cm}^{-3}} = \alpha + \beta \left(\frac{r}{\text{pc}} \right), \quad (2)$$

where β is the gradient of the profile. The center of nebula is identified as the position of the peak flux of $H\alpha$. The best-fit parameters are listed in Table 3.

The derived density gradient changes by using different methods of the measurement. LMC N191 and SMC N88A have evident negative density gradients with a slope of $-75 \text{ cm}^{-3} \text{ pc}^{-1} < \beta < -45 \text{ cm}^{-3} \text{ pc}^{-1}$ for LMC N191 and $-850 \text{ cm}^{-3} \text{ pc}^{-1} < \beta < -175 \text{ cm}^{-3} \text{ pc}^{-1}$ for SMC N88A. In LMC N191, the density gradient derived from the K19 [O II]-ratio method is smaller than the gradient derived from other methods. In contrast, the SMC N77A and SMC N456 have the shallow and even flat density gradients. In SMC N77A, the density gradient derived from the [S II]-ratio is marginally negative by $-8 \pm 5 \text{ cm}^{-3} \text{ pc}^{-1} < \beta < -6 \pm 5 \text{ cm}^{-3} \text{ pc}^{-1}$. The gradient derived from the [O II]-ratio is flat with a $\beta \sim 4 \pm 5.5 \text{ cm}^{-3} \text{ pc}^{-1}$. In SMC N456, the density gradient is flat within the error range by $\beta \sim -3 \pm 3 \text{ cm}^{-3} \text{ pc}^{-1}$.

5.2. Temperature structures

In Figure 9, we present the maps of electron temperatures derived from [O III]-ratio through the methods given by Osterbrock & Ferland (2006) and (Nicholls et al. 2020). The temperature is evenly distributed across the entire nebula for the four HII regions.

We calculate the average and the standard deviation of T_e of each HII region. As shown in Table 2, the average temperature of the HII region is around 8000 K to 13000 K, which is consistent with the previous measurement from the integrated spectra (Testor et al. 2003; Peña-Guerrero et al. 2012a; Selier & Heydari-Malayeri

2012). In each nebula, the measured temperature is consistent between the OF06 method and the NKS20 method.

We derive the temperature gradient of each HII region by fitting temperature radial profiles with an analytical function as below,

$$\frac{T_e}{\text{K}} = \alpha + \beta \left(\frac{r}{\text{pc}} \right), \quad (3)$$

where r is the radius of nebula. The center of nebula is identified as the position of the peak flux of $H\alpha$. The best-fit parameters are listed in table 3.

The temperature gradient is flat in the four HII regions. The gradient is negligible to the average temperature of each nebula by $\beta \approx 5\% < T_e >$, where $< T_e >$ is the measured average temperature. LMC N191, SMC N77A and SMC N88A show a positive trend in the temperature radial profile with the gradient ranging from $37 \pm 41 \text{ K pc}^{-1}$ to $180 \pm 320 \text{ K pc}^{-1}$. SMC N456 shows a negative trend in the temperature radial profile with a gradient of $-27 \pm 30 \text{ K pc}^{-1}$. The gradient values are smaller than the fitting errors in the four nebulae.

6. COMPARISON TO MODELS

We combined stellar atmosphere models with the MAPPINGS V photoionization code to create a set of HII region models. The modeled HII regions have a broad range of ionization parameter and pressure.

6.1. Stellar ionizing source

Ionizing sources of each HII region are identified through the photometry of stars. In LMC N191, the dominant star is a $M_V = -5.27 \text{ mag}$ O-star, of which the spectral type is classified as O5 V (Selier & Heydari-Malayeri 2012). The ionizing source in SMC N77A is suggested as an early-type B-star with an intrinsic color of $B-V = -0.28$ (Selier & Heydari-Malayeri 2012). Testor et al. (2003) suggest that the ionizing source in SMC N88A has a spectral type of O6-O8 V star with a M_V of -4.85. The stellar context in SMC N456 is complex because it contains four bright O-type stars, with M_V ranging from -4.5 to -4.75 mag (Testor & Lortet 1987).

We use the ionizing spectra from the TLUSTY stellar atmosphere library (Hubeny & Lanz 1995, 2017) for our photoionization models. The TLUSTY models are fully consistent, non-LTE (local thermodynamic equilibrium) line-blanketed atmosphere models allowing a broad range of effective temperature from 10 K to 10^8 K. We use the stellar atmosphere models with [Fe/H] abundance of -1.0 for the SMC nebulae and -0.7 for the LMC nebulae (Cioni 2009).

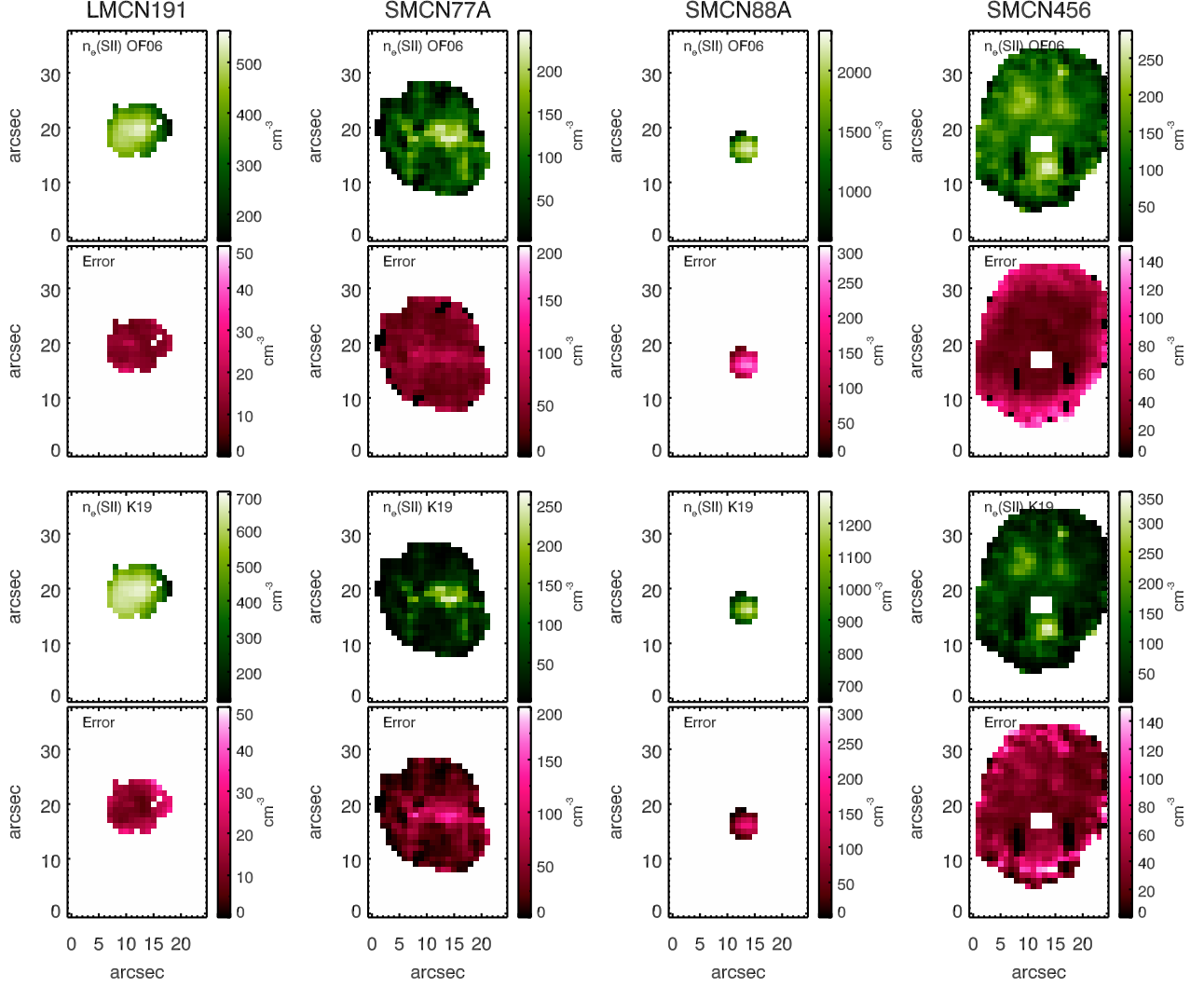


Figure 7. Maps of electron density n_e . The color code indicates the value of n_e . **First row:** Maps of the electron density derived from the [S II] ratio based on the method in Osterbrock & Ferland (2006). **Second row:** Maps of errors of the electron density derived from the [S II] ratio based on the method in Osterbrock & Ferland (2006). **Third row:** Maps of the electron density derived from the [S II] ratio based on the method in Kewley et al. (2019a). **Fourth row:** Maps of errors of the electron density derived from the [S II] ratio based on the method in Kewley et al. (2019a).

Table 2. The average and standard deviation of the temperature by pixels of each HII region

(K)	LMCN191	SMCN77A	SMCN88A	SMCN456
$\langle T_e \rangle_{OF06}$	8864	11405	12932	11321
$\sigma(T_e)_{OF06}$	813	630	1763	423
$\langle T_e \rangle_{NKS20}$	8923	11490	13030	11405
$\sigma(T_e)_{NKS20}$	823	636	1779	427

6.2. Photoionization model grid

We used the MAPPINGS V photoionization code (Binette 1985; Sutherland & Dopita 1993; Dopita et al. 2013) for modeling the ISM in compact HII regions. MAPPINGS V code utilizes the latest CHIANTI v.8.0

atomic database (Del Zanna et al. 2015) for the lightest 30 elements.

MAPPINGS V is a photoionization code which is used to calculate the thermal and ionization structures of the ISM plasma with the equilibrium of cooling and heating, excitation and de-excitation. MAPPINGS V gener-

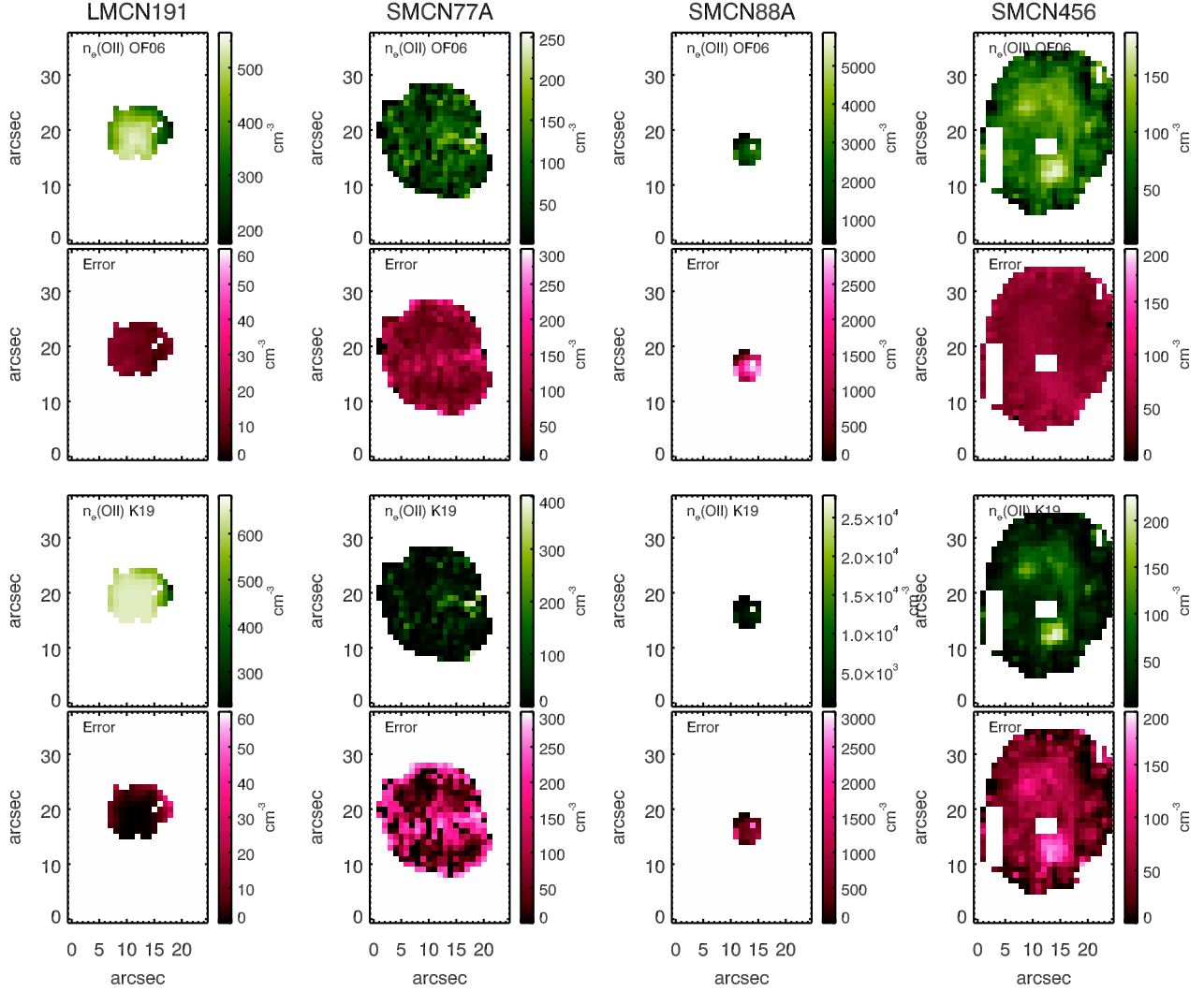


Figure 8. Maps of electron density n_e . The color code indicates the value of n_e . **First row:** Maps of the electron density derived from the [O II] ratio based on the method in Osterbrock & Ferland (2006). **Second row:** Maps of errors of the electron density derived from the [O II] ratio based on the method in Osterbrock & Ferland (2006). **Third row:** Maps of the electron density derived from the [O II] ratio based on the method in Kewley et al. (2019a). **Fourth row:** Maps of errors of the electron density derived from the [O II] ratio based on the method in Kewley et al. (2019a).

ates the nebular radial variation of the electron density, temperature, the ionic fraction and the emissions of 30 elements, under the assumption of the ISM density and pressure structure across the nebula. MAPPINGS calculates the radiation from two components, the ionizing source and the ionizing recombination emission. The fractional contribution of each component is determined based on the nebular geometry.

We construct the photoionization model grid with a set of constant ISM pressures ranging from $\log(P/k)=5$ to $\log(P/K)=9$ in a step of 0.05 dex, a set of ionization parameters from $\log(Q)=6.0$ to $\log(Q)=9.5$ in a step of 0.125 dex, and a varying stellar effective temperatures from $T_{\text{eff}}=30\,000$ K to $T_{\text{eff}}=50\,000$ K in a step

of 2500 K. Compared with the isochoric model which assumes a constant ISM density, constant ISM pressure is a more realistic assumption to the majority of HII regions where the heating and cooling timescales are longer than the sound-crossing time (Field 1965; Begelman & McKee 1990).

We use the spherical geometry models for our comparison. MAPPINGS is designed to generate the plane-parallel and spherical nebular models. The plane-parallel models are usually applied to the nebula whose radius is far larger than its thickness, while the spherical models are used for the cloud powered by a point source at its center. Our observed four HII regions have a round shape, with both LMC N191 and SMC N88A

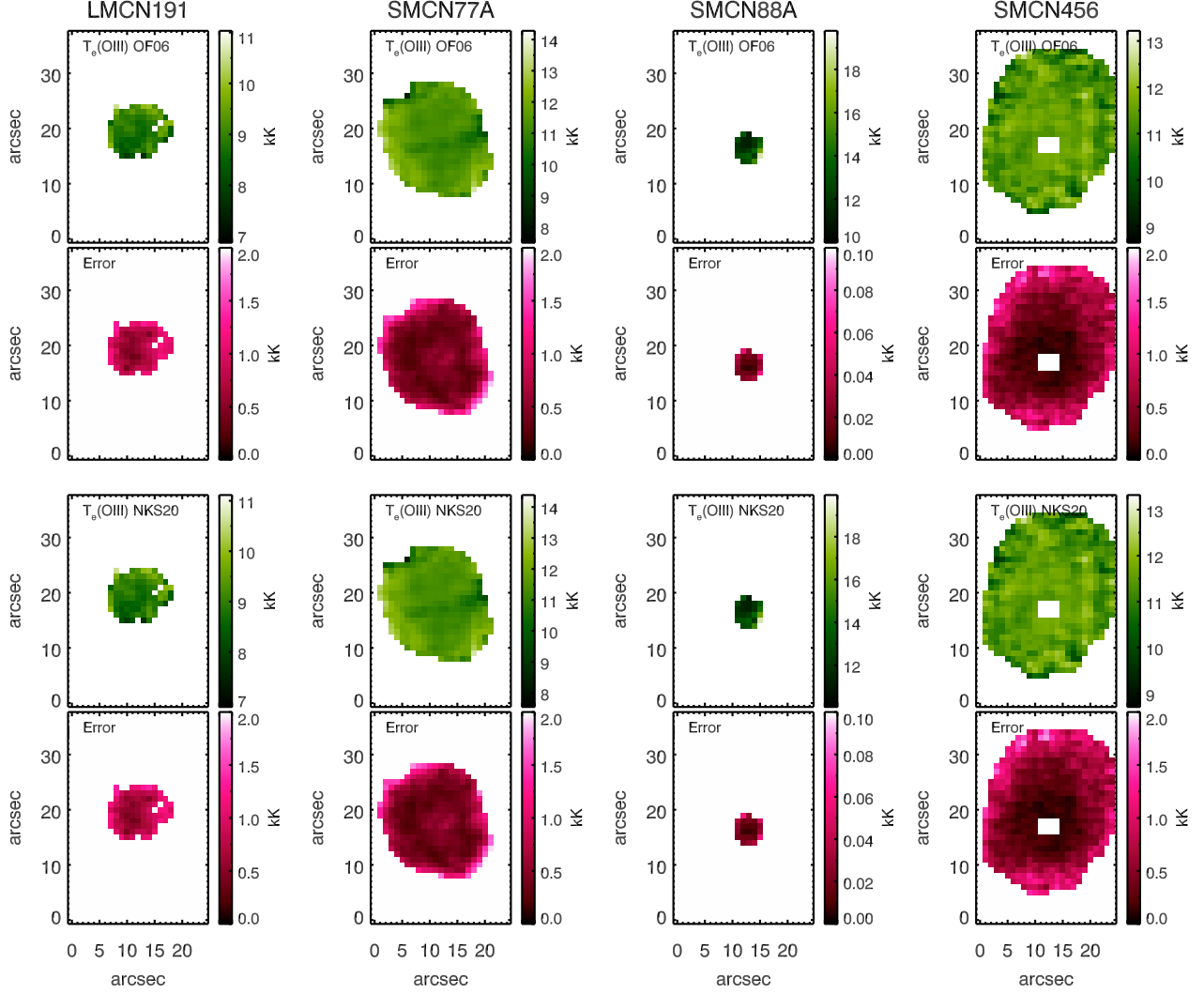


Figure 9. Maps of electron temperature T_e . The color code indicates the value of T_e . **First row:** Maps of electron temperature derived from the [O III] ratio based on the method in Osterbrock & Ferland (2006). **Second row:** Maps of the error of electron temperature measured from the [O III] ratio based on the method in Osterbrock & Ferland (2006). **Third row:** Maps of electron temperature derived from the [O III] ratio based on the method in Nicholls et al. (2020). **Fourth row:** Maps of the error of electron temperature measured from the [O III] ratio based on the method in Nicholls et al. (2020).

appearing spherical. Therefore the spherical geometry is more appropriate than plane parallel geometry for our HII regions.

The ISM in the Magellanic Clouds have a non-solar element ratio which cannot be simply derived by scaling the solar metallicity. We used the measured ISM metallicity in Magellanic Clouds from Russell & Dopita (1992). In general, the mean metallicity of the LMC is 0.2 dex lower than our Galactic ISM, while the SMC has a metallicity 0.6 dex lower. We included 15 elements in our LMC model and 16 elements in our SMC model. The details of element abundances are listed in Table 4

6.3. Iterative Searching process

We take a three-step fitting process to determine the best-fit model of the global emission-line spectrum of each HII region. The global spectrum is integrated across the entire field-of-view. First, we use a coarse model grid to fit the temperature-sensitive line ratios, $[\text{N II}]\lambda\lambda 6548,84/[\text{N II}]\lambda 5755$, $[\text{O III}]\lambda 5007/[\text{O III}]\lambda 4363$, to roughly estimate the temperature of nebula and derive the theoretical full hydrogen spectrum based on the temperature. The selected temperature-sensitive line ratios are free from dust extinction. The $[\text{N II}]\lambda\lambda 6548,84/[\text{N II}]\lambda 5755$ ratio traces the temperature of the low-ionization zone of the nebula. The $[\text{O III}]\lambda 5007/[\text{O III}]\lambda 4363$ ratio traces the temperature of the high-ionization zone of the nebula.

Table 3. Parameters of the best-fits to the radial profiles of electron temperature and electron density^a.

	LMC N191		SMC N77A		SMC N88A		SMC N456	
	α	β	α	β	α	β	α	β
$T_e(OIII)$								
(OF06)	8570±256	73±87	11117±156	37±41	12299±7	179±317	11610±252	-27±30
$T_e(OIII)$								
(NKS20)	8626±259	75±88	11200±157	37±41	12391±8	181±320	11697±253	-27±31
$n_e(SII)$								
(OF06)	582±21	-54±5	143±49	-8±5	2375±179	-396±117	156±45	-3±3
$n_e(SII)$								
(K19)	748±17	-72±6	88±51	-6±5	1276±96	-172±40	112±52	-3±3
$n_e(OII)$								
(OF06)	579±13	-46±5	107±37	-4±5	3033±717	-722±353	115±30	-3±3
$n_e(OII)$								
(K19)	655±2	-5±2	73±54	-4±6	3244±483	-831±189	61±38	-2±4

^a The radial profiles are fitted with the analytical function $\frac{y}{K/cm^{-3}} = \alpha + \beta \left(\frac{r}{pc}\right)$, where y is the electron temperature or the electron density, α is the intercept of the radial profile and β is the gradient of the radial profile.

The coarse model grid has $5 < \log P/K < 9$ in a step of 0.5dex, $6 < \log Q < 9.5$ in 0.5dex steps and $30\,000\text{ K} < T_{\text{eff}} < 50\,000\text{ K}$ in a step of 25000 K.

Then, we perform the extinction correction by comparing the full hydrogen spectrum between the selected model and the observation. The extinction correction based on the Balmer decrement of $H\alpha/H\beta=2.86$, needs to assume the nebula is optically thick with a constant temperature of 10^4 K (the Case-B nebula). Instead, we fit the full hydrogen spectrum by using the Hydrogen emission-lines simultaneously, which is free from the arbitrary Case B assumption. The observed fluxes and the best-fit model fluxes of the hydrogen spectrum are listed in Table 5 to Table 8.

The extinction correction is taken by converting the intensity of emission-lines, $I(\lambda)$, to the intrinsic intensity, $I_0(\lambda)$, through the equation below.

$$I_0(\lambda) = I(\lambda) \times 10^{C_n \times f(\lambda)}, \quad (4)$$

where C_n is the logarithmic nebula reddening constant and $A(\lambda)/AV$ is the attenuation curve proposed by (Fitzpatrick 1999). $f(\lambda)$ is the extinction function normalized by $H\beta$ $f(\lambda) = A(\lambda)/AV / (Av/A(H\beta) - 1)$, to avoid the difference between the stellar extinction function and the nebular extinction function.

Finally, we search for the best-fit model of the de-reddened emission-line spectrum by using the fine model grid described in Section 6.2. The best-fit model is identified with the minimal χ^2 value, where χ^2 is defined as below,

$$\chi^2 = \sqrt{\sum_{\lambda} \left(\frac{F_{\lambda}^{Obs} - F_{\lambda}^{Mod}}{F_{\lambda}^{Obs}} \right)^2}, \quad (5)$$

where F_{λ}^{Obs} and F_{λ}^{Mod} are observed and modeled fluxes used at each step.

6.3.1. Best-fit model

Table 9 presents the R_v and C_n for each nebula. The R_v of SMC N77A and LMC N191 are consistent with the $R_v = 2.93$ of the Small Magellanic Cloud and $R_v = 3.16$ of the Large Magellanic Cloud (Pei 1992) within an error of $\sim 6\%$. The R_v of SMC N88A and SMC N456 are larger than the R_v of the SMC.

Table 10 presents the derived parameters of the best-fit model. These four nebulae have the central stellar temperature of $37\,500\text{ K} < T_{\text{eff}} < 46\,500\text{ K}$. The ionization parameter of the nebulae in SMC is $8.125 < \log(Q_H) < 9.250$, which are larger than the typical ionization parameter $7 < \log(Q_H) < 8$ of local HII regions

Table 4. The abundance of the LMC and the SMC from Russell & Dopita (1992)

Element	SMC	
	LMC	SMC
	log(X/H)	log(X/H)
H	0.0	0.0
He	-1.05	-1.09
C	-3.96	-4.24
N	-4.86	-5.37
O	-3.65	-3.97
Ne	-4.39	-4.73
Na	-4.85	-5.92
Mg	-4.53	-5.01
Al	–	-5.60
Si	-4.28	-4.69
S	-5.29	-5.41
Cl	-7.23	-7.30
Ar	-5.71	-6.29
Ca	-6.03	-6.16
Fe	-4.77	-5.11
Ni	-6.04	-6.14

(Dopita et al. 2000). The nebula in LMC has an ionization parameter of 7.625 falling in the range of ionization parameters of typical local HII regions. The ISM pressure is $6.0 < \log(P/k) < 7.4$ of these four nebulae.

The electron temperature of nebula derived from the best-fit model is $9000\text{K} < T_e < 14500\text{K}$ and consistent with the volume-weighted average temperature, $T_e[\text{O III}]$, measured from the IFU data. The temperature of LMC N191 is 9270K , matching with the measured temperature of $8864 \pm 813\text{K}$. The temperatures of SMC N77A and SMC N456 are close to the typical assumption of $T_e = 10000\text{K}$ of an ideal "Case B" nebula model. The SMC N77A has the temperature of $T_e = 11860\text{K}$ consistent with the measured temperature $T_e = 11405 \pm 630\text{K}$. The SMC N456 has the derived temperature of $T_e = 12540\text{K}$ in agreement with the measured temperature $T_e = 113215 \pm 423\text{K}$. The SMC 88A has the hottest temperature in the sample, with a derived temperature $T_e = 14170\text{K}$ consistent with the measured temperature of $T_e = 12932 \pm 1763\text{K}$.

The density of the nebula derived from the best-fit model is $10\text{cm}^{-3} < n_e < 10^3\text{cm}^{-3}$. The SMC N77A has the lowest density of $n_e = 43\text{cm}^{-3}$. The LMC N191 and SMC N456 have the density of $n_e = 339\text{cm}^{-3}$ and

114cm^{-3} respectively. The SMC N88A is the densest nebula with a density of $n_e = 1016\text{cm}^{-3}$.

6.4. Emission-line Ratios

Table 11 presents the comparison of the key integrated line-ratios between the observations and the best-fit model. We compare the ionization-parameter-sensitive line-ratio $[\text{O III}]\lambda\lambda 4959,5007/[\text{O II}]\lambda\lambda 3726,27$ (the well-known O32 ratio), the temperature-sensitive line-ratio $[\text{O III}]\lambda 4363/[\text{O III}]\lambda\lambda 4959,5007$, and the density-sensitive line-ratios $[\text{O II}]\lambda 3726/[\text{O II}]\lambda 3729$ and $[\text{S II}]\lambda 6716 / [\text{S II}]\lambda 6731$. We use $\Delta\%$ to measure the derivation of the best-fit line-ratios from the observation. $\Delta\%$ is described as below,

$$\Delta\% = \frac{|F_\lambda^{Obs} - F_\lambda^{Mod}|}{F_\lambda^{Obs}} \times 100, \quad (6)$$

where F_λ^{Obs} and F_λ^{Mod} are observed and modeled fluxes.

The density-sensitive $[\text{O II}]$ -ratio and $[\text{S II}]$ -ratio are well-fitted with the $\Delta\%$ smaller than 10%. The goodness of the temperature-sensitive line-ratio fitting varies from the $\Delta\%$ of 0.71% in SMC N88A to the $\Delta\%$ of 24.04% in SMC N456. The $\Delta\%$ of the $[\text{O III}]/[\text{O II}]$ ratio ranges from 10-15%.

Figure 10 presents the comparison of the radial profile of the temperature-sensitive line-ratio, $[\text{O III}]\lambda 4363/[\text{O III}]\lambda 5007$, and the density-sensitive line-ratios, $[\text{O II}]\lambda 3727/[\text{O II}]\lambda 3729$ and $[\text{S II}]\lambda 6717/[\text{S II}]\lambda 6731$, between the best-fit model and the observation. The distance to the center of nebula is normalized by the maximal radius of the nebula, R_{max} . We project the 3D spherical nebula onto a 2D plane in order to compare with the observation. The line-ratio at each distance is the integration along the line-of-sight direction.

The constant pressure model predicts that the $[\text{O II}]\lambda 3727/[\text{O II}]\lambda 3729$ ratio is an increasing function of the distance to the center of nebula. In contrast, the observation shows that the $[\text{O II}]$ -ratio decreases along the distance to the center of nebula for LMC N191 and SMC N456. In SMC N77A and SMC N88A, the median value of the $[\text{O II}]$ -ratio displays a decreasing trend along the distance to the nebular center although the measurement error of 25-50% on the $[\text{O II}]$ -ratio is too large to reveal an evident gradient of the radial profile.

The observations show that the $[\text{S II}]\lambda 6717 / [\text{S II}]\lambda 6731$ ratio increases with the distance to the center of nebula for the four HII regions. In contrast, the modeled $[\text{S II}]$ -ratio displays a flat distribution within the nebula. The discrepancy of the $[\text{S II}]$ -ratio between the model and the observation reveals that the density structure of the nebula is more complex than the current models.

The temperature-sensitive $[\text{O III}]\lambda 4363/[\text{O III}]\lambda 5007$ ratio profiles are flat in the four HII regions, which are

Table 5. LMC N191 Hydrogen Spectrum De-Reddened and Residuals

Wavelength (Å)	Obs. Flux (H β = 100)	Error 1 σ %	De-Red Obs. Flux	De-Red Model	Diff. %
3734.375	2.427	0.91	2.740	2.397	12.52
3750.158	3.046	1.39	3.433	3.048	11.21
3770.637	3.775	1.43	4.246	3.963	6.66
3835.391	6.563	1.56	7.330	7.292	0.52
3970.079	14.89	0.79	16.40	15.86	3.29
4101.742	24.42	0.65	26.53	25.83	2.64
4340.471	44.03	0.19	46.68	46.74	0.13
4861.333	100.00	0.94	100.00	100.00	0.00
6562.819	331.05	0.23	285.02	287.73	0.95
8437.956	0.477	0.70	0.370	0.317	14.32
8467.254	0.567	0.44	0.439	0.376	14.35
8502.483	0.639	1.22	0.494	0.450	8.91
8665.019	1.188	1.83	0.913	0.839	8.11
8750.472	1.518	1.62	1.163	1.068	8.17
8862.782	1.925	2.99	1.468	1.389	5.38

Table 6. SMC N77A Hydrogen Spectrum De-Reddened and Residuals

Wavelength (Å)	Obs. Flux (H β = 100)	Error 1 σ %	De-Red Obs. Flux	De-Red Model	Diff. %
3734.375	2.445	2.05	2.558	2.401	6.14
3750.158	2.950	1.32	3.084	3.059	0.81
3770.637	3.739	1.02	3.906	3.980	1.89
3835.391	6.730	0.66	7.012	7.336	4.62
3970.079	14.78	0.62	15.32	15.97	4.24
4101.742	25.04	0.34	25.82	25.99	0.66
4340.471	43.30	0.37	44.23	47.00	6.26
4861.333	100.00	0.59	100.00	100.00	0.00
6562.819	369.47	0.26	350.20	284.45	18.77
8437.956	0.334	2.91	0.307	0.307	0.15
8467.254	0.423	2.13	0.389	0.365	6.17
8502.483	0.418	3.72	0.385	0.437	13.51
8665.019	0.826	1.32	0.758	0.817	7.78
8750.472	1.135	1.98	1.041	1.041	0.03
8862.782	1.547	0.94	1.418	1.354	4.51

consistent with the measurements of the flat temperature gradients in nebula. In contrast, the constant pressure models predict a decreasing [O III]-ratio profile for the four HII regions.

6.5. The pressure of nebula

Figure 11 presents the radial profile of the pressure of the four HII regions. For each nebula, the pressure, $\log(P/k)$, is calculated by using four different indicators.

- $\log(P/k)_{[\text{SII}]}^{OF06}$ is calculated by using T_e measured by the Osterbrock & Ferland (2006) method and $n_{e[\text{SII}]}$ derived from [S II]-ratio by using the Osterbrock & Ferland (2006) method,
- $\log(P/k)_{[\text{SII}]}^{K19}$ is calculated by using T_e measured by the Osterbrock & Ferland (2006) method and $n_{e[\text{SII}]}$ derived from [S II]-ratio by using the Kewley et al. (2019a) method,

Table 7. SMC N88A Hydrogen Spectrum De-Reddened and Residuals

Wavelength (Å)	Obs. Flux (H β = 100)	Error 1 σ %	De-Red Obs. Flux	De-Red Model	Diff. %
3734.375	2.010	1.04	2.591	2.392	7.68
3750.158	2.531	0.79	3.253	3.050	6.24
3770.637	2.994	0.78	3.832	3.970	3.60
3835.391	5.696	0.59	7.196	7.324	1.78
3970.079	13.20	0.32	16.23	15.95	1.73
4101.742	22.89	0.16	27.38	25.97	5.15
4340.471	42.41	0.27	48.23	47.13	2.28
4861.333	100.00	0.36	100.00	100.00	0.00
6562.819	471.06	0.21	327.41	283.07	13.54
8437.956	0.727	0.70	0.316	0.300	5.06
8467.254	0.881	0.26	0.381	0.355	6.82
8502.483	1.040	0.70	0.446	0.426	4.48
8665.019	1.832	0.25	0.759	0.795	4.74
8750.472	2.398	0.23	0.977	1.012	3.58
8862.782	3.147	0.13	1.255	1.316	4.86

Table 8. SMC N456 Hydrogen Spectrum De-Reddened and Residuals

Wavelength (Å)	Obs. Flux (H β = 100)	Error 1 σ %	De-Red Obs. Flux	De-Red Model	Diff. %
3734.375	2.334	0.54	2.556	2.401	6.06
3750.158	2.989	0.84	3.269	3.059	6.42
3770.637	3.812	0.62	4.162	3.981	4.35
3835.391	6.726	0.47	7.307	7.339	0.44
3970.079	14.54	0.24	15.64	15.98	2.17
4101.742	24.20	0.13	25.76	26.00	0.93
4340.471	43.36	0.44	45.32	47.05	3.82
4861.333	100.00	0.43	100.00	100.00	0.00
6562.819	341.59	0.43	304.33	283.79	6.75
8437.956	0.439	21.00	0.356	0.305	14.33
8467.254	0.542	1.11	0.438	0.362	17.35
8502.483	0.577	13.50	0.466	0.434	6.87
8665.019	0.976	4.73	0.783	0.811	3.58
8750.472	1.403	0.51	1.123	1.032	8.10
8862.782	1.343	2.36	1.070	1.344	25.61

- $\log(P/k)_{[\text{OII}]}^{OF06}$ is calculated by using T_e measured by the Osterbrock & Ferland (2006) method and $n_{e[\text{OII}]}$ derived from [O II]-ratio by the Osterbrock & Ferland (2006) method,
- $\log(P/k)_{[\text{OII}]}^{K19}$ is calculated by using T_e measured by the Osterbrock & Ferland (2006) method and $n_{e[\text{OII}]}$ derived from [O II]-ratio by the Kewley et al. (2019a) method,

The radial profiles of $\log(P/k)$ shows an isobaric condition within the nebula. In SMC N77A, SMC N88A and SMC N456, the pressure has a flat distribution across the nebula. In LMC N191, the pressure has a flat gradient within $0.7R_{max}$ and decreases from $0.7R_{max}$ to $1R_{max}$. The average pressure of the nebula ranges from $5.4 \pm 1.1 < \log(P/k) < 7.7 \pm 0.36$, which is consistent with the range of pressures predicted by the best-fit models.

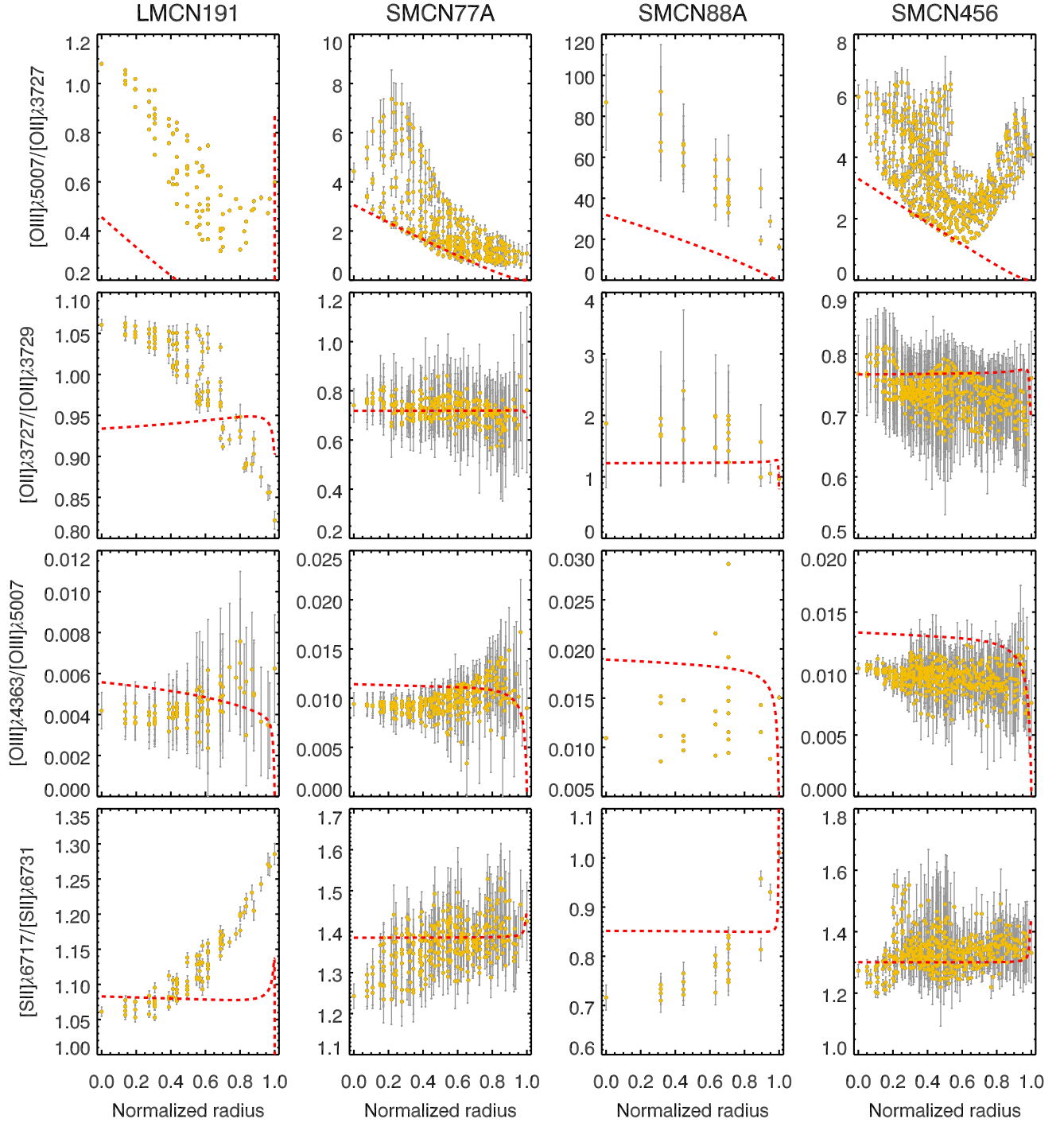


Figure 10. The comparison of radial distribution of the density-sensitive and the temperature-sensitive line ratios between our observational data and our constant pressure models. Each row presents the radial distribution of each individual H II region. The line ratios are the projection along the line-of-sight directions. The radius is normalized to the maximum radius of models for the constant pressure models and is normalized to the maximum radius of the nebula for the observed data. **Left:** The comparison of the radial distribution of the density-sensitive line ratio of $[S\ II]\lambda 6716/[S\ II]\lambda 6731$. **Middle:** The comparison of the radial distribution of the density-sensitive line ratio of $[O\ II]\lambda 3727/[O\ II]\lambda 3729$. **Left:** The comparison of the radial distribution of the temperature-sensitive line ratio of $[O\ III]\lambda 5007/[O\ III]\lambda 4363$. In each panel, the black points are the observed data and the lines present the radial distribution of $[S\ II]\lambda 6716/[S\ II]\lambda 6731$ given by constant pressure models with different $\log(P/k)$ and ionization parameters.

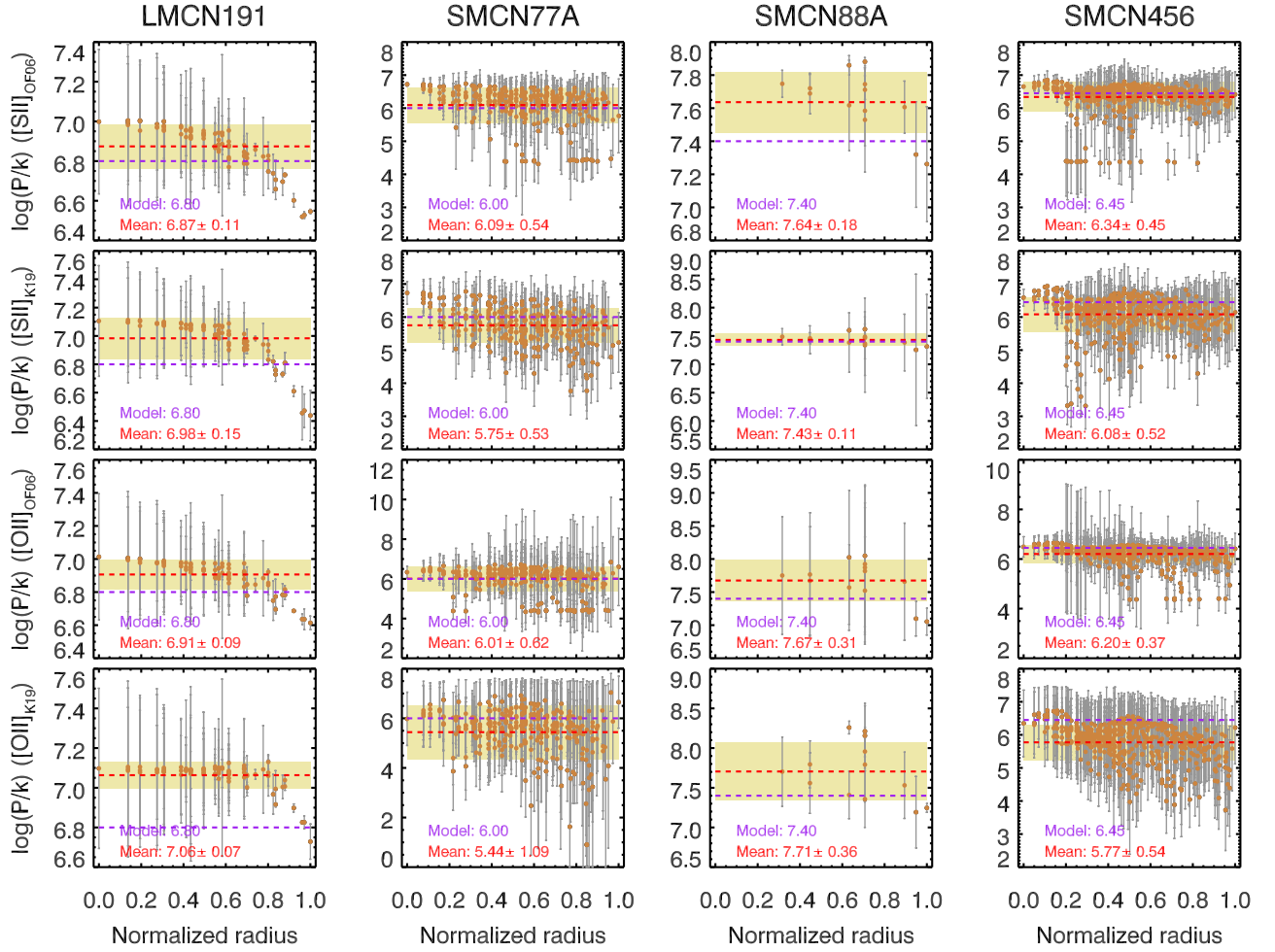
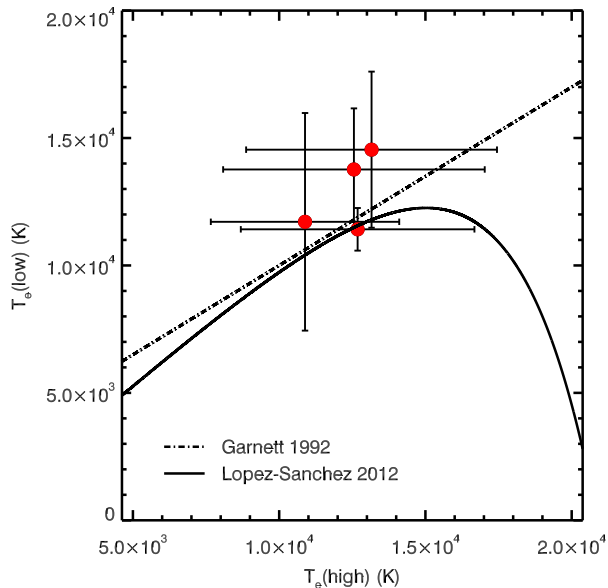


Figure 11. The ISM pressure profiles of the HII regions. The pressure is derived through $P/k = 2n_e(1 + He/H)T_e$. The radius is normalized to the maximum radius of models for the constant pressure models and is normalized to the maximum radius of the nebula for the observed data. The red dashed line indicates the average of the derived pressure. The purple dashed line indicates the modeled pressure value. The yellow region indicates the 1σ of the measured pressure.

Table 9. Global Spherical Isobaric Derived Reddening Parameters.

HII Region	R _v	C _n (dex)
LMC N191	3.41	0.200
SMC N77A	2.74	0.061
SMC N88A	6.49	0.771
SMC N456	4.02	0.174

**Figure 12.** Comparison of the electron temperature of high-ionization species and the temperature of low-ionization species. The temperature of high-ionization species is measured from the $[\text{O III}]\lambda 5007/[\text{O III}]\lambda 4363$ ratio. The temperature of low-ionization species is measured from the $[\text{N II}]\lambda\lambda 6548,84/[\text{N II}]\lambda 5755$ ratio. The solid line is the relationship given by López-Sánchez et al. (2012) and the dot-dashed line is the relationship induced by Garnett (1992).

7. DISCUSSION

7.1. Temperature Structures of HII regions

The electron temperature is a crucial diagnostic for determining the ISM metallicity. Calibrations of metallicity are derived from simple photoionization models with constant temperature or density. However, real HII regions are composed of multi-ionization zones with fluctuations of temperatures and densities (Garnett 1992). In our data, HII regions have two distinct zones: a high-ionization zone and a low-ionization zone. The high-ionization zone with high-ionization species, like Ne^{2+} and O^{2+} , is located closer to the central star than the

low-ionization zone with low-ionization species, like O^+ and N^+ , within nebula. This is because the stellar radiation field is absorbed in regions closer to the central star so that there are few ionizing photons to ionize atoms to high ionization stages in the outer regions of the nebula.

Analyses of integrated nebular spectra suggest that electron temperatures vary from a low-ionization zone to a high-ionization zone (Peimbert 1967; Peimbert et al. 2004, 2017). The lines $[\text{O III}]\lambda 4363$, $[\text{O III}]\lambda\lambda 4959, 5007$ are most often used for determining the temperature in HII regions. However, the temperature derived from the $[\text{O III}]$ lines, $T_e(\text{OIII})$, only represents the temperature in the O^{2+} zones. Hägele et al. (2008) suggest that the missing T_e in low-ionization zones can lead to an underestimate of the metallicity by 0.2 dex. A two-ionization zone model is assumed to convert the T_e in high-ionization zones to the T_e in low ionization zones. As shown in Figure 12, our HII region sample suggests that the observed relationship of average temperatures in high-ionization zones and low-ionization zones matches with the analytical function given by previous research (Garnett 1992; López-Sánchez et al. 2012).

In contrast to the assumption of constant temperature in photoionization models, real HII regions have radial variations of electron temperatures. Detailed study of the θ^1 Ori C area in the Orion nebula demonstrates that the electron temperature rises with distance from the ionizing star (Rubin et al. 2011). Our data show a sign of the positive gradient of the temperature profiles within LMC N191, SMC N77A and SMC N88A. However, the uncertainties of the best-fit gradients are too large to exclude the possibility of a flat or negative gradient of the temperature profiles within these HII regions. SMC N456 shows a sign of a negative gradient of the temperature profile but the uncertainty of the best-fit gradient is too large to exclude a positive or flat gradient. The electron temperature gradient causes an underestimate of the derived metallicity calibration (Stasińska 2005) and can cause the difference between metallicities calibrated from recombination lines and auroral lines (Peimbert et al. 2017).

The inhomogeneity of the electron temperature within HII regions is attributed to several main mechanisms (Peimbert et al. 2017). One mechanism is the extreme density inhomogeneity leading to the low-temperature heavily shadowed area within HII regions. The second mechanism is the temperature inhomogeneity is the mechanical energy input by stellar winds and shocks (Arthur et al. 2016; O’Dell et al. 2017). Another potential cause of temperature inhomogeneities is the spatial distribution of multiple ionizing sources within HII regions.

Table 10. Global Spherical Isobaric Nebula Derived Properties

HII Region	$\log(Q_H)$ (cm s^{-1})	$T_{\text{src.}}$ (K)	$\log(P/k)$	Fe Depl. (dex)	$\langle T_e \rangle$ (K)	$\langle n_e \rangle$ (cm^{-3})
LMC N191	7.625	37 500	6.80	0.5	9 274	339
SMC N77A	8.125	38 500	6.00	1.0	11 860	43
SMC N88A	9.250	46 500	7.40	1.5	14 360	1 016
SMC N456	8.125	38 500	6.45	1.5	12 540	114

Table 11. Key line-ratios of the nebulae and the best-fit models.

	$[\text{O III}]/[\text{O II}]$ (5007+4959)/(3726+3729)	$[\text{O III}]/[\text{O III}]$ 4363/(5007+4959)	$[\text{O II}]/[\text{O II}]$ 3726/3729	$[\text{S II}]/[\text{S II}]$ 6716/6731
LMC-N191	0.332	0.0035	0.90	1.15
$\sigma\%$	1.19	0.99	0.92	0.22
Model	0.291	0.0041	0.93	1.08
$\Delta\%$	12.3	17.1	3.3	6.1
SMC N77A	1.378	0.00754	0.724	1.344
$\sigma\%$	0.97	0.81	0.75	0.42
Model	1.179	0.00800	0.719	1.385
$\Delta\%$	14.45	6.13	0.71	3.07
SMC N88A	15.144	0.01415	1.236	0.875
$\sigma\%$	1.86	0.34	1.84	0.5
Model	13.499	0.0140	1.232	0.849
$\Delta\%$	10.86	0.71	0.32	2.97
SMC N456	1.899	0.00795	0.759	1.298
$\sigma\%$	0.93	0.45	0.86	0.19
Model	1.604	0.00987	0.767	1.301
$\Delta\%$	15.55	24.04	1.13	0.2

7.2. Density Structures of HII regions

Most HII region models assume constant density across the nebula. However, the constant density assumption is not realistic given that real HII regions have significant density variations. The density variations are found to be 80-700 cm^{-3} in the Orion nebula (Rubin et al. 2011) and to be 40-4000 cm^{-3} within HII regions in the inner region of the Milky Way (Simpson et al. 2004).

The density radial gradients are complex in nearby HII regions. The measurement of electron densities across the θ^1 Ori C area shows that the density variation is not a monotonic function of distance to the ionizing star (Rubin et al. 2011). In large nearby HII

regions, the density gradients are observed to be flat (García-Benito et al. 2010; Ramos-Larios et al. 2010) while the density gradients appear to be negative in compact HII regions (Binette et al. 2002; McLeod et al. 2016). Particularly, ultra-compact HII regions have the steepest density gradients among all categories of nebulae (Kurtz 2002; Johnson & Kobulnicky 2003; Phillips 2007).

Our observed HII regions also show a large range of density gradients. The density gradient is as steep as around $-700 \text{ cm}^{-3} \text{ pc}^{-1}$ in SMC N88A. However, the density gradients can also be as flat as $-3 \text{ cm}^{-3} \text{ pc}^{-1}$ in SMC N456.

Diverse density gradients of HII regions are attributed to complex nebular geometry. In the Orion nebula, complex density gradients are likely the result of a turbulent HII region (Arthur et al. 2016; Ha et al. 2021) with bar-like structures (van der Werf et al. 2013; Rubin et al. 2011), where the contamination of scattered light from dense clumps change the electron density distribution (Kewley et al. 2019b).

There are two major processes proposed that create complex density structures within HII regions. One is the “collect and collapse” scenario (Elmegreen et al. 1995), where dense clumps are formed when HII regions expand into turbulent ISM. The other is the “radiation driven implosion” model (Bertoldi 1989), where overdensities within HII regions are amplified by the heating of hot stars. Both processes create an overdensity of the ISM (Walch et al. 2015; Schneider et al. 2016). The stellar wind is another potential cause for the complex geometries of HII regions (Park et al. 2010).

7.3. Pressure structures of HII regions

The ISM pressure is a key parameter to describe the ISM properties, which includes both nebular temperature and density structures. The ISM pressure is determined by the mechanical energy produced by stellar feedback, the strength and the shape of the radiation field. Models with a constant ISM pressure are more realistic than models with a constant density or temperature, when the sound-crossing timescale is shorter than the heating and cooling timescale. Previous research shows that the condition of constant pressure occurs within the majority of HII regions (Begelman & McKee 1990; Gutiérrez & Beckman 2010).

The value of ISM pressure crosses a broad interval in HII region models (Kewley et al. 2019a,b), ranging from a low pressure of $\log(P/k)=4$ to a high pressure environment with $\log(P/k)=8-9$ which is observed in high-redshift HII regions (Lehnert et al. 2009). Our sampled HII regions in the LMC and the SMC present ISM pressures around $\log(P/k)=6-8$, which is consistent with the range given by models.

7.4. Implications for future photoionization models

Self-consistent photoionization models, like CLOUDY and MAPPINGS, require as input an assumption of the shape of the nebula. Constant temperature or density assumptions are always applied to simple photoionization models but this is not physically realistic. Our observations reveal that the substructures, as filaments or dense knots, exist within real HII regions, which are caused by stellar winds, ISM turbulence and the nebular expansion. Our observations indicate that the temperature and density structures do not obey the isothermal

or constant density assumptions. Gradients of temperature and density structures exist in the LMC and SMC nebulae. Allowing temperature and density to vary results in a more physically realistic model.

To model realistic HII regions, some approximations of nebular geometries are applied. Some studies have used plane-parallel approximations to mimic the behavior of non-spherical structures in nebula (Levesque et al. 2010), and some use concentric shells to deal with the shell-like structures within HII regions (Pellegrini et al. 2020). In these models, the contribution of the diffuse ionizing photons to the ionization field is assumed as a fixed fraction, which may bear no relation to a real nebula with complex geometries.

Fully self-consistent three-dimensional photoionization codes are needed. Monte-Carlo radiative transfer techniques offer the promise of a substantial improvement over current simple structures to handle the complex geometry of nebulae. Some Monte-Carlo photoionization codes are already available (Ercolano & Bastian 2008; Vandenbroucke & Wood 2018) and have shown promise in modeling the ionized gas around young stars (Law et al. 2011) and nebulae with filamentary structures (Ercolano et al. 2012). For a precise modeling of nebular emission-lines and internal structures, a Monte-Carlo code with comprehensive considerations of atomic data and ISM microphysics, like cooling and heating processes, is under development. The new code incorporates the Monte-Carlo radiative transfer technique into the existing MAPPINGS photoionization code and will be presented in a forthcoming paper (Jin et al. in prep.)

This research was supported by the Australian Research Council Centre of Excellence for All Sky Astrophysics in 3 Dimensions (ASTRO 3D), through project number CE170100013. L.J.K. gratefully acknowledges the support of an ARC Laureate Fellowship (FL150100113).

REFERENCES

- Arellano-Córdova, K. Z. & Rodríguez, M. 2020, *MNRAS*, 497, 672. doi:10.1093/mnras/staa1759
- Arthur, S. J., Medina, S.-N. X., & Henney, W. J. 2016, *MNRAS*, 463, 2864
- Begelman, M. C. & McKee, C. F. 1990, *ApJ*, 358, 375. doi:10.1086/168994
- Bertoldi, F. 1989, *ApJ*, 346, 735. doi:10.1086/168055
- Binette, L. 1985, *A&A*, 143, 334
- Binette, L., González-Gómez, D. I., & Mayya, Y. D. 2002, *RMxAA*, 38, 279
- Childress, M. J., Vogt, F. P. A., Nielsen, J., et al. 2014, *Ap&SS*, 349, 617
- Cioni, M.-R. L. 2009, *A&A*, 506, 1137
- Chu, Y.-H., & Kennicutt, R. C. 1986, *ApJ*, 311, 85
- Copetti, M. V. F., Mallmann, J. A. H., Schmidt, A. A., et al. 2000, *A&A*, 357, 621
- Del Zanna, G., Dere, K. P., Young, P. R., et al. 2015, *A&A*, 582, A56
- Dopita, M. A., Kewley, L. J., Heisler, C. A., et al. 2000, *ApJ*, 542, 224. doi:10.1086/309538
- Dopita, M., Hart, J., McGregor, P., et al. 2007, *Ap&SS*, 310, 255
- Dopita, M., Rhee, J., Farage, C., et al. 2010, *Ap&SS*, 327, 245
- Dopita, M. A., Sutherland, R. S., Nicholls, D. C., et al. 2013, *ApJS*, 208, 10
- Dopita, M. A., Seitenzahl, I. R., Sutherland, R. S., et al. 2016, *ApJ*, 826, 150. doi:10.3847/0004-637X/826/2/150
- Dopita, M. A., Vogt, F. P. A., Sutherland, R. S., et al. 2018, *ApJS*, 237, 10. doi:10.3847/1538-4365/aac837
- Dopita, M. A., & Seitenzahl, I. 2019, *Supernova Remnants: An Odyssey in Space After Stellar Death II*, 4
- Elmegreen, B. G., Kimura, T., & Tosa, M. 1995, *ApJ*, 451, 675. doi:10.1086/176253
- Ercolano, B., & Bastian, N. 2008, *Mass Loss from Stars and the Evolution of Stellar Clusters*, 397
- Ercolano, B., Dale, J. E., Gritschneider, M., et al. 2012, *MNRAS*, 420, 141
- Field, G. B. 1965, *ApJ*, 142, 531. doi:10.1086/148317
- Fitzpatrick, E. L. 1999, *PASP*, 111, 63
- Filippenko, A. V. 1985, *ApJ*, 289, 475
- García-Benito, R., Díaz, A., Hägele, G. F., et al. 2010, *MNRAS*, 408, 2234
- Garnett, D. R. 1992, *AJ*, 103, 1330. doi:10.1086/116146
- Garnett, D. R., Skillman, E. D., Dufour, R. J., et al. 1995, *ApJ*, 443, 64. doi:10.1086/175503
- Garnett, D. R., & Dinerstein, H. L. 2001, *ApJ*, 558, 145
- Gordon, K. D., Clayton, G. C., Misselt, K. A., et al. 2003, *ApJ*, 594, 279. doi:10.1086/376774
- Groves, B. A., Dopita, M. A., & Sutherland, R. S. 2004, *ApJS*, 153, 75
- Gutiérrez, L. & Beckman, J. E. 2010, *ApJL*, 710, L44. doi:10.1088/2041-8205/710/1/L44
- Ha, T., Li, Y., Xu, S., et al. 2021, *ApJL*, 907, L40. doi:10.3847/2041-8213/abd8c9
- Hägele, G. F., Pérez-Montero, E., Díaz, Á. I., et al. 2006, *MNRAS*, 372, 293
- Hägele, G. F., Díaz, Á. I., Terlevich, E., et al. 2008, *MNRAS*, 383, 209
- Henize, K. G. 1956, *ApJS*, 2, 315. doi:10.1086/190025
- Herrera-Camus, R., Bolatto, A., Smith, J. D., et al. 2016, *ApJ*, 826, 175
- Hubeny, I., & Lanz, T. 1995, *ApJ*, 439, 875
- Hubeny, I., & Lanz, T. 2017, *arXiv e-prints*, arXiv:1706.01859
- Jin, Y., Kewley, L. J., & Sutherland, R. S. 2022, *ApJL*, 934, L8. doi:10.3847/2041-8213/ac80f3
- Johnson, K. E. & Kobulnicky, H. A. 2003, *ApJ*, 597, 923. doi:10.1086/378585
- Johnstone, C. P., Güdel, M., Lüftinger, T., et al. 2015, *A&A*, 577, A27. doi:10.1051/0004-6361/20142530010.48550/arXiv.1503.06669
- Kennicutt, R. C. 1984, *ApJ*, 287, 116
- Kennicutt, R. C., & Hodge, P. W. 1986, *ApJ*, 306, 130
- Kewley, L. J., Nicholls, D. C., Sutherland, R., et al. 2019, *ApJ*, 880, 16
- Kewley, L. J., Nicholls, D. C., & Sutherland, R. S. 2019, *ARA&A*, 57, 511
- Kollmeier, J. A., Zasowski, G., Rix, H.-W., et al. 2017, *arXiv e-prints*, arXiv:1711.03234
- Krabbe, A. C., & Copetti, M. V. F. 2002, *A&A*, 387, 295
- Kumari, N., James, B. L., & Irwin, M. J. 2017, *MNRAS*, 470, 4618
- Kurtz, S. 2002, *Hot Star Workshop III: The Earliest Phases of Massive Star Birth*, 267, 81
- Law, K.-H., Gordon, K. D., & Misselt, K. A. 2011, *ApJ*, 738, 124
- Lehnert, M. D., Nesvadba, N. P. H., Le Tiran, L., et al. 2009, *ApJ*, 699, 1660
- Levesque, E. M., Kewley, L. J., & Larson, K. L. 2010, *AJ*, 139, 712
- Liu, X.-W., Barlow, M. J., Zhang, Y., et al. 2006, *MNRAS*, 368, 1959
- López-Sánchez, Á. R., Dopita, M. A., Kewley, L. J., et al. 2012, *MNRAS*, 426, 2630. doi:10.1111/j.1365-2966.2012.21145.x

- Malmann, J. A. H., Copetti, M. V. F., Dos Santos, I. C. F., et al. 2002, *Revista Mexicana De Astronomia Y Astrofisica Conference Series*, 57
- Mendoza, C. 1983, *Planetary Nebulae*, 103, 143
- McLeod, A. F., Gritschneider, M., Dale, J. E., et al. 2016, *MNRAS*, 462, 3537. doi:10.1093/mnras/stw1864
- Nicholls, D. C., Kewley, L. J., & Sutherland, R. S. 2020, *PASP*, 132, 033001. doi:10.1088/1538-3873/ab6818
- O'Dell, C. R., Ferland, G. J., & Peimbert, M. 2017, *MNRAS*, 464, 4835
- Osterbrock, D. E. 1989, *Astrophysics of Gaseous Nebulae and Active Galactic Nuclei*
- Osterbrock, D. E., & Ferland, G. J. 2006, *Astrophysics of gaseous nebulae and active galactic nuclei*
- Park, J.-W., Min, K.-W., Seon, K.-I., et al. 2010, *ApJ*, 719, 1964. doi:10.1088/0004-637X/719/2/1964
- Pei, Y. C. 1992, *ApJ*, 395, 130. doi:10.1086/171637
- Peimbert, M. 1967, *ApJ*, 150, 825
- Peimbert, M. & Torres-Peimbert, S. 1976, *ApJ*, 203, 581. doi:10.1086/154114
- Peimbert, M., Peimbert, A., Ruiz, M. T., et al. 2004, *ApJS*, 150, 431
- Peimbert, M., Peimbert, A., & Delgado-Inglada, G. 2017, *PASP*, 129, 082001. doi:10.1088/1538-3873/aa72c3
- Pellegrini, E. W., Rahner, D., Reissl, S., et al. 2020, *MNRAS*, doi:10.1093/mnras/staa1473
- Peña-Guerrero, M. A., Peimbert, A., Peimbert, M., et al. 2012, *ApJ*, 746, 115
- Peña-Guerrero, M. A., Peimbert, A., & Peimbert, M. 2012, *ApJL*, 756, L14
- Phillips, J. P. 2007, *MNRAS*, 380, 369. doi:10.1111/j.1365-2966.2007.12078.x
- Ramos-Larios, G., Phillips, J. P., & Pérez-Grana, J. A. 2010, *MNRAS*, 405, 245. doi:10.1111/j.1365-2966.2010.16483.x
- Rubin, R. H., Simpson, J. P., Lord, S. D., et al. 1994, *ApJ*, 420, 772
- Rubin, R. H., Simpson, J. P., O'Dell, C. R., et al. 2011, *MNRAS*, 410, 1320. doi:10.1111/j.1365-2966.2010.17522.x
- Rubin, R. H., Simpson, J. P., Colgan, S. W. J., et al. 2016, *MNRAS*, 459, 1875
- Russell, S. C., & Dopita, M. A. 1992, *ApJ*, 384, 508
- Schneider, N., Bontemps, S., Motte, F., et al. 2016, *A&A*, 591, A40. doi:10.1051/0004-6361/201628328
- Selier, R., & Heydari-Malayeri, M. 2012, *A&A*, 545, A29
- Simpson, J. P., Rubin, R. H., Colgan, S. W. J., et al. 2004, *ApJ*, 611, 338. doi:10.1086/422028
- Stasińska, G. 2005, *A&A*, 434, 507
- Stasińska, G., Morisset, C., Simón-Díaz, S., et al. 2013, *A&A*, 551, A82
- Sutherland, R. S., & Dopita, M. A. 1993, *ApJS*, 88, 253
- Testor, G. & Lortet, M.-C. 1987, *A&A*, 178, 25
- Testor, G., Lemaire, J. L., & Field, D. 2003, *A&A*, 407, 905
- Testor, G., Lemaire, J. L., Heydari-Malayeri, M., et al. 2010, *A&A*, 510, A95. doi:10.1051/0004-6361/200911786
- Toribio San Cipriano, L., Domínguez-Guzmán, G., Esteban, C., et al. 2017, *MNRAS*, 467, 3759. doi:10.1093/mnras/stx328
- van der Werf, P. P., Goss, W. M., & O'Dell, C. R. 2013, *ApJ*, 762, 101. doi:10.1088/0004-637X/762/2/101
- Vandenbroucke, B., & Wood, K. 2018, *Astronomy and Computing*, 23, 40
- Vermeij, R., & van der Hulst, J. M. 2002, *A&A*, 391, 1081
- Walch, S., Girichidis, P., Naab, T., et al. 2015, *MNRAS*, 454, 238. doi:10.1093/mnras/stv1975